Storm-induced turbidity currents on a sediment-starved shelf: Insight from direct monitoring and repeat seabed mapping of upslope migrating bedforms

Alexandre Normandeau, Daniel Bourgault, Urs Neumeier, Patrick Lajeunesse, Guillaume St-Onge, Louis Gostiaux, Cédric Chavanne

SEDIMENTOLOGY
the journal of the International Association of Sedimentologists

Upslope migrating bedforms during storm-induced turbidity currents: Insights from direct monitoring and repeat seabed mapping of a sediment-starved shelf

Journal:	*Sedimentology*
Manuscript ID	SED-2018-TP-281.R1
Manuscript Type:	Original Manuscript
Date Submitted by the Author:	18-Jun-2019
Complete List of Authors:	Normandeau, Alexandre; Natural Resources Canada, Geological Survey of Canada (Atlantic); Natural Resources Canada Bourgault, Daniel; Universite du Quebec Institut des sciences de la mer de Rimouski Neumeier, Urs; Universite du Quebec Institut des sciences de la mer de Rimouski Lajeunesse, Patrick ; Université aval, Géographie St-Onge, Guillaume; Universite du Quebec Institut des sciences de la mer de Rimouski Gostiaux, Louis; Université de Lyon Chavanne, Cédric; Universite du Quebec Institut des sciences de la mer de Rimouski
Keywords:	Cyclic steps, Turbidity currents, St. Lawrence Estuary, Bedforms, Monitoring, ADCP, seabed mapping
Note: The following files were submitted by the author for peer review, but cannot be converted to PDF. You must view these files (e.g. movies) online.	
Supp_Mat_1_PDM_2007-2017.gif Supp_Mat_2_Gully_2007-2017.gif	

Upslope migrating bedforms during storm-induced turbidity currents: Insights from direct monitoring and repeat seabed mapping of a sediment-starved shelf

Alexandre Normandeau[1], Daniel Bourgault[2], Urs Neumeier[2], Patrick Lajeunesse[3], Guillaume St-Onge[2], Louis Gostiaux[4], Cédric Chavanne[2]

[1] *Geological Survey of Canada – Atlantic, 1 Challenger Drive, Dartmouth, Nova Scotia, B2Y 4A2, Canada*

[2] *Institut des sciences de la mer de Rimouski, Université du Québec à Rimouski, Rimouski, Québec G5L 3A1, Canada*

[3] *Centre d'études nordiques & Département de géographie, Université Laval, 2405 Rue de la Terrasse, Québec, Québec G1V 0A6, Canada*

[4] *Univ Lyon, École Centrale de Lyon, INSA Lyon, Université Claude Bernard Lyon I, CNRS, Laboratoire de Mécanique des Fluides et d'Acoustique, UMR 5509, 36 Avenue Guy de Collongue, F-69134, ECULLY, France*

ABSTRACT

The monitoring of turbidity currents enables accurate internal structure and timing of these flows to be understood. Without monitoring, the triggers of turbidity currents often remain hypothetical and based on sedimentary structures of deposits and their age. In this study, the bottom currents within 20 m of the seabed in one of the Pointe-des-Monts (Gulf of St. Lawrence, eastern Canada) submarine shelf canyons were monitored for two consecutive years using Acoustic Doppler Current Profilers (ADCP). In addition, multibeam bathymetric surveys were carried out during the ADCPs deployment and recovery operations. These new surveys, along with previous multibeam surveys carried out over the last decade, revealed that crescentic bedforms have migrated upslope by about 20-40 m since 2007, despite the limited supply of sediment on the shelf or river inflow in the region. During the winter of 2017, two turbidity currents with velocities reaching 0.5 and 2 m s^{-1}, respectively, were recorded and were responsible for the rapid (less than 1 minute) upstream migration of crescentic bedforms observed between the autumn surveys of 2016 and 2017. The 200 kg mooring was also displaced 10 m downcanyon, up the stoss side of a bedform, suggesting that a dense basal layer was driving the flow during the first minute of the event. Two other weaker turbidity currents with speeds <0.5 ms^{-1} occurred, but did not lead to any significant change on the seabed. These four turbidity currents coincided with strong and sustained wind speed > 60 km h^{-1} and higher than normal wave heights. Repeat seabed mapping suggests that the turbidity currents cannot be attributed to a canyon-wall slope failure. Rather, sustained windstorms triggered turbidity currents either by remobilizing limited volumes of sediment on the shelf or by resuspending sediment in the canyon head. Turbidity currents can thus be triggered when sediment volume available is limited, likely by eroding and incorporating canyon thalweg sediment in the flow,

thereby igniting the flow. This process appears to be particularly important for the generation of turbidity currents capable of eroding upslope migrating bedforms in sediment-starved environments. Turbidity currents may thus be triggered by storms in environments with very low sediment supply when canyons heads are shallow and the slope is steep, which might have wider implications for the activity of submarine canyons worldwide.

INTRODUCTION

Turbidity currents are gravity flows that transfer large volumes of sediment and organic carbon to the deep-sea (e.g., Azpiroz-Zabala et al., 2017a). They represent major geohazards since they can break communication cables, subsea pipelines, and oil and gas infrastructures (Heezen & Ewing, 1952; Carter et al., 2014). The knowledge of where, when and how they occur is of prime importance to mitigate their impact (Bruschi et al., 2006). More importantly, a complete understanding of their impact on the seafloor is critical for the management of seabed infrastructures. Because there are relatively few locations worldwide with direct observations of turbidity currents (e.g., *Monterey Canyon*: Xu et al., 2014, 2012, Paull et al., 2003, 2018; *La Jolla and Scripps Canyon*: Shepard and Marshall, 1973, Inman et al., 1976; *Squamish delta*: Hughes Clarke, 2016, Hizzet et al., 2017, Hage et al., 2018; *Bute Inlet*: Prior et al., 1987, Zeng et al., 1991, Bornhold et al., 1994; *Congo Canyon*: Khripounoff et al., 2003, Cooper et al., 2013, Azpiroz-Zabala et al., 2017a; *Fraser delta*: Ayranci et al., 2012, Lintern et al., 2016; *Gaoping Canyon*: Zhang et al., 2018, *Mendocino Canyon*: Sumner et al., 2014) and that most studies were not able to associate seafloor morphological change with precise turbidity current events (Hizzet et

al., 2017; Hage et al., 2018; Paull et al., 2018), the factors responsible for triggering them and their direct and precise effect on the seafloor are poorly known and understood.

Puig et al. (2013) identified four main triggers of turbidity currents: 1) hyperpycnal flows; 2) submarine slope failures; 3) advection of shelf sediments or cyclic loading of shelf sediment inducing failure during strong wave action; and 4) bottom trawling. In addition, internal tides, internal waves and dense shelf water cascades are known to transport sediment downcanyon (Puig et al., 2004, 2008). More recently, detailed work on the Squamish delta (British Columbia, Canada) revealed that river-generated turbidity currents and delta-front slope failures produce significant change on the seafloor (Clare et al, 2016; Hizzett et al., 2017; Hughes Clarke, 2016). Hughes Clarke et al. (2014) and subsequent studies on the Squamish delta demonstrated that direct plunging of hyperpycnal flows does not occur on the delta front, but that the settling of river plumes transforms into turbidity currents. This process, referred to as plume settling events (Hizzett et al., 2017), may be more prevalent on delta fronts than the direct plunging of hyperpycnal flows and may share similar characteristics with the advection of shelf sediment during storms that generate turbidity currents (Piper & Normark, 2009). These uncertainties about turbidity current triggers demonstrate that much remains to be understood about the process by which turbidity currents are generated and how they shape the seafloor during their passage.

In this study, we examine a peculiar type of submarine canyons/channels in which turbidity currents have been inferred from past repeat bathymetric surveys (Normandeau et al., 2014) (Fig. 1A). We present a 10-year monitoring program that includes repeat bathymetric surveys combined with a 2-year Acoustic Doppler Current Profiler (ADCP) mooring that measured velocity profile and acoustic backscatter that is a proxy for suspended sediment

to examine: 1) when and how turbidity currents are triggered in a sediment-starved shelf environment; 2) how turbidity currents evolve from initiation by storms to deposition; and 3) how different behaviours of turbidity currents shape the seabed and are responsible for the evolution of a turbidite system. This study sheds new light on the mechanisms responsible for triggering turbidity currents and how different turbidity current behaviours modify the seabed.

REGIONAL BACKGROUND

The St. Lawrence Estuary is among the largest estuaries in the world and was glacially-carved during past glaciations, forming the Laurentian Channel. The Laurentian Channel is >300 m deep in some locations and is bounded by steep slopes (often ≥5°), favouring the presence of submarine landslides (Pinet et al., 2015) and submarine channels (Normandeau et al., 2015). Submarine channels were largely active during deglaciation, when ice-margin retreat provided large volumes of sediment to the marine environment (Dietrich et al., 2016, 2017; Normandeau et al., 2017). Other incisions on the slope, defined as submarine canyons to differentiate them from channels observed offshore rivers, were found to be episodically active today (>100 year recurrence) (Normandeau et al., 2017).

The submarine canyons that experienced frequent turbidity current activity are, counterintuitively, those located off Pointe-des-Monts with little sediment supply at their head, with bedrock exposed on the shelf (Fig. 1; 49°18' N 67°23' W). These canyons are located less than 300 m from the shoreline and have a length of 4.5 km. Their width varies between 100 to 300 m. The upper slope of the Pointe-des-Monts canyons is steep, with values reaching 20° where bedrock is exposed, decreasing downslope to 2-3° in the thalweg where bedforms are present. Normandeau et al. (2014) showed that 30-60 m long bedforms

within the canyons migrated upslope by 5-25 m between 2007 and 2012 in 200 m water depth despite the limited volume of sediment on the shelf feeding the canyon heads (Fig. 2). The shores also have minimal sediment, as demonstrated by satellite images where small pocket beaches located close to the canyon heads directly overly bedrock (Fig. 2).

The hydrodynamic environment of the St. Lawrence Estuary is driven mainly by the semi-diurnal tides (3 m tidal range), river runoff and wind (Koutitonsky and Bugden, 1991). The interaction of hydrodynamics and complex bathymetry leads to the formation of internal tides and internal waves in the estuary (e.g., Saucier and Chassé, 2000), which are known to impact sediment transport processes (Bourgault et al., 2014).

METHODS

The Pointe-des-Monts Observatory

The Pointe-des-Monts observatory began in 2012, when preliminary investigations revealed that bedforms migrated in the canyons between 2007 and 2012 (Normandeau et al., 2014). Repeat multibeam bathymetric surveys were subsequently conducted in June 2015, August, September and October 2016 and October 2017 (Fig. 1C) using a 200-300 kHz Kongsberg EM2040 and corrected for tides and water column sound velocity. The data were referenced to chart datum. The horizontal resolution of the data is 2 x 2 m and the vertical resolution varies from 0.1 m in shallow water to 0.5 m in deeper areas of the seafloor. Therefore, sediment deposition smaller than 0.5 m at the base of the canyons/channels cannot be imaged.

Near-bottom currents and water temperatures were measured at one location within the Pointe-des-Monts shelf canyons for approximately 26 consecutive months, but with a 10-

week gap in the data record (Fig. 1C). A first mooring was deployed between 3 June 2015 and 1 August 2016. A second mooring was deployed between 12 October 2016 and 12 October 2017. Both were installed at 49°18.4' N / 67°23.5' W in a water depth of 187 m from the R/V Coriolis II. The moorings were deployed in the most active canyon and were positioned to accurately capture turbidity currents coming down from any of the upstream gullies (Fig. 1). The second mooring, which recorded the turbidity currents presented in this study, consisted of 300 kg train wheels, 2 buoys of 11 kg each at 5 m of chain, an acoustic release, 2 buoys of 11kg each at 6 m above bottom, followed by a steel cable with the Acoustic Doppler Current Profiler (ADCP) in a steel frame at 22 m and a 140 kg buoy at 30 m above bottom (Fig. 1D). Total weight in water of mooring is about 200 kg. Both moorings were equipped with a 600 kHz Workhorse Sentinel ADCP which measured water velocities and a RBR duet pressure-depth sensor. ADCPs were positioned at, respectively, 31 m and 22 m above bottom (mab) and their acoustic beams pointed downward with a 20° angle respective to a vertical line. Near the seabed, side lobe interference leads to invalid velocity data in the bottom 1 m. Their pinging period was set to 25 s and 20 s. All pings were recorded individually without ensemble averaging. The vertical bin size was 1 m. To reduce random noise, the raw velocity data were low-pass filtered with a moving average filter with 9 points to produce 3 min averages. Backscatter intensity was corrected for spherical spreading loss, sound attenuation taking into account temperature, ping frequency, battery voltage, and estimated salinity. The ADCP recorded only small roll and tilt variations during the entire mooring deployment, neither of which went beyond -2.5° and 2° from the vertical.

154 The height of the second ADCP above the seabed (22 m) and its acoustic beam spread of
155 20° insonifies a diameter of 16 m of the seabed. Each of the four 20° tilted ADCP beams
156 was used as an echosounder to map the seafloor morphology on an 8-m radius circle around
157 the ADCP with a vertical resolution of 1 cm (1% of ADCP bin size). For each ping, a
158 parabolic curve was fitted to the backscatter intensity profile and the seafloor position
159 calculated using the beam orientation measured by the ADCP compass. As the ADCP was
160 turning slowly on its axis by 120° to 180° with each tide, data covered the full circle and
161 could be averaged for each 5° sector. These 360° data were compared to the multibeam
162 data to extract the exact location of the ADCP after deployment and recovery of the
163 mooring.

164 When deploying and recovering the ADCPs, multibeam bathymetric surveys were
165 conducted to associate seafloor morphological change to currents observed with the ADCP
166 (Fig. 1C).

167 **Wave and weather data**

168 The significant surface wave heights (*H*) and mean wave period (*T*) were measured with
169 an Acoustic Wave and Current profiler with Acoustic Surface Tracking (AWAC-AST) 600
170 kHz at Saint-Ulric (48°48.0' N 67°44.6' W, 60 km south of Pointe-des-Monts; Fig. 1A)
171 between 20 October 2016 and 31 May 2017 and at Rivière-Pentecôte (49°41.8' N 67°08.6'
172 W, 45 km north-east of Pointe-des-Monts; Fig. 1A) between 27 October 2016 and 6 June
173 2017. These instruments, installed in 30 m water depth, also measured sea ice thickness.
174 These instruments, although not located at the Pointe-des-Monts site, provide an estimation
175 of surface wave conditions in the estuary during storms. The waver levels measured by

these instruments were used to compute storm surges by subtracting the tide prediction obtained with t_tide (Pawlowicz et al., 2002)

Hourly atmospheric measurements of wind and air temperature were obtained from the Historical Climate Data of the Government of Canada at the terrestrial weather station Pointes-des-Monts (49°19.20' N, 067°22.80' W and 5.9 m altitude; Fig. 1B). Sea ice conditions were obtained from the daily ice charts produced by the Canadian Ice Service.

RESULTS

A decade of seafloor morphological change

Crescentic bedforms (30-60 m wavelength, 1-3 m waveheigth) have been identified in the Pointe-des-Monts canyons in previous years and have migrated upslope between 2007 and 2012 (Normandeau et al., 2014). The upslope migration of crescentic bedforms is characterized by sediment erosion on the lee side and deposition on the stoss (Fig. 3). New bathymetric data collected in 2015 to 2017 also show that a net change occurred from 2012 to 2017 by the upslope migration of the crescentic bedforms (Fig. 3, Supp. vid. 1-3). Upslope migration commonly ranged between 1 and 40 m from 2012 to 2017 (mean = 20 m). Most notably, between 2012 and 2015, crescentic bedforms in the gullies located to the East of the canyons migrated (Fig. 4). These gullies directly offlap bedrock at their head at 165 m water depth (Fig. 4C). No visible slope failures occurred on the channel walls or at the head of those gullies during most of that period, nor at the head of the canyons (Figs. 3-4). However, between 2015 and 2017, a significant bathymetric change occurred in one of the gullies, likely due to a small slope failure (~150 000 m^3), which led to up to 17 m of erosion on the gully's head and up to 7 m of sediment deposition in the gully itself (Fig. 3A).

During the 2015-2016 period, no changes on the seafloor of the main canyon were observed; i.e., crescentic bedforms did not migrate (Fig. 1C). However, during the 2016-2017 period, crescentic bedforms migrated upslope (1-12 m) in the main canyon where the ADCP was located (Fig. 3C).

During the 10 year period, migration of bedforms was most frequent in the main canyon, where the ADCP was moored. Migration of bedforms was mostly restricted to the upper to mid canyon (Fig. 3A). No migration of bedforms was observed down on the lobe. Similarly, when bedforms migrated in the eastern gullies, they were restricted to the confined part. Conversely, when flows occurred in the middle canyon, migration of bedforms could be observed down to the proximal part of the lobe (Fig. 3A).

Turbidity current monitoring

Combining the observation of backscatter (echo intensity), which is due to sound reflection on particles (in this case, suspended sediment), and velocity over the period 2015-2017, four turbidity currents were identified and occurred during the 2016-2017 period (Fig. 5, Supplementary Fig. 1). Turbidity currents were identified by their high values of backscatter signal in combination with a sharp increase in down-canyon velocity. Two of the four turbidity currents are discussed in more detail in the present study: the 15 March 2017 and 25 January 2017 events.

The fastest turbidity current was measured on 15 March 2017 at 12:51:49 UTC and is associated with the largest near-bottom backscatter intensity and the largest bottom currents of the entire two years of monitoring (Figs. 5-6). Currents in the canyon at 1.4 mab prior to the turbidity current were around 0.1 m s^{-1} up-canyon (Fig. 6). Current horizontal velocity reached a maximum down-canyon velocity of 2.2 m s^{-1} during the turbidity

current. Temperature at 22 mab increased from 3°C to 4°C at turbidity current arrival before decreasing back to 3°C 15 minutes later (Fig. 6I). This event lasted about 70 minutes during which three distinct and consecutive pulses occurred with different flow directions that were oriented up to 90° of the canyon axis (Fig. 6B-D). One possibility to explain the three main pulses is that the turbidity currents were triggered at the same time in different upslope channels. If this was the case, at a velocity of 2 m s^{-1}, the peaks should be separated by 1-4 minutes (length to mooring of 450 m for the closest channel head compared to 870 m for the farthest one). However, given that the peaks were separated by 30 minutes, the turbidity current more likely consisted of multiple pulses. The oblique directions of the flow can either be due to the sharp turn in the canyons axis, which leads to helical flows around meander bends (e.g., Azpiroz-Zabala et al., 2017b) or to the shape of the crescentic bedforms that permits flows to travel obliquely on the sides of the canyon. The velocity peaks are coincident with peaks in backscatter in the water column, indicative of peaks in suspended sediment concentration (Fig. 6A-B, K-L). Backscatter intensities then remained higher than normal for a few hours until most sediment settled in the canyon. Fine sediment, however, appears to have remained in suspension following the event for several weeks. This turbidity current was the thickest of the year, the cloud of suspended sediment reaching a height distinctly more than 20 m (the height of the ADCP) but with a main body of 4-10 m where current speed is noticeably faster, above 1 ms^{-1} (Fig. 6B, E). The direction of currents within the turbidity currents also reveals the structure of the flow where the lower 10 m show homogeneity in current direction compared to the upper parts of the flow that show strong variations (Fig. 6C). These variations are likely associated with mixing and water entrainment. During the beginning of the second pulse, which was the fastest

one at > 2 m s^{-1}, the depth of the ADCP measured by a pressure sensor (0.01 m accuracy) suddenly changed, moving upwards by 0.7 m in less than 20 s (Figs. 5E, 6J).

The 25 January 2017 turbidity current was the second fastest of the two years. It is characterized by a sharp increase in backscatter near the bottom coincident with a sharp down-canyon increase in velocity to 0.55 m s^{-1} at 1.4 mab (Fig. 7A-D). Compared to the 15 March event, this turbidity current had only one pulse that lasted about 20 minutes. It reached a thickness of 20 m although the main body was 4-6 m thick with higher velocities and a homogenous current direction (Fig. 7B-C). The dilute upper layer mixes with ambient water and likely leads to water entrainment in the flow. The ADCP does not show any change in depth although the distance from ADCP to seafloor shows a sudden accumulation of around 0.1 m (Figs. 5E, 7J) following this event.

Two other low velocity turbidity currents were triggered on 12 November 2016 and 4 January 2017. These turbidity currents were slower and hardly discernible from the background velocities along canyon (Fig. 5G), although velocity data were temporarily unavailable at the head of these turbidity currents. On 12 November 2016, three backscatter pulses of turbidity currents lasting less than 60 minutes each occurred separated by 1-2 hours. The maximum measured velocity attained by these turbidity currents were around 0.35 m s^{-1}.

Atmospheric conditions during the turbidity currents

All four turbidity currents were initiated during storms that affected eastern Canada and during higher than normal wind speed and wave height (Supplementary Table 1-3, Fig. 5). The two fastest turbidity currents were triggered during strong wind from Northeast (> 70 km h^{-1}; Supplementary Table 1). However, other storms, some with stronger wind speeds

and greater wave height than those that triggered the turbidity currents, had little to no effect on bottom velocities in the canyon (e.g., 30 December 2016; Supplementary Table 1-3, Fig. 5). The duration of strong winds appears to be more important for triggering turbidity currents than the maximum wind speed recorded (Fig. 8A-D). A common characteristic of the storms that triggered turbidity currents is that wind speeds reached > 60 km h^{-1} (Supplementary Table 1). Examining all storms where wind speed reached more than 60 km h^{-1} suggests that sustained wind speed may be an additional factor required for triggering turbidity currents (Fig. 8A-D). There is no significant difference between storms that triggered turbidity currents and those that did not when looking at the duration of wind speed > 40 km h^{-1} during the storms (Fig. 8A). However, a significant difference becomes apparent when examining the duration of wind speed above 60 km h^{-1} (Fig. 8C). Turbidity currents were triggered when wind speeds reached > 60 km h^{-1} continuously for more than 7 hours. Those sustained wind speeds of 7 hours that did not trigger turbidity currents were not continuous, i.e., wind speed varied between > 60 km h^{-1} and 40 km h^{-1} for more than 10 hours. Wind speed reaching above 70 km h^{-1} occurred at other times but lasted less than 7 hours (Fig. 8D). During three of the four turbidity currents, storm surges dues to low pressures occurred. However, storm surges also occurred during storms that did not trigger turbidity currents such as 30 December 2016, with a storm surge of 1.24 m.

Although continuous and sustained wind speeds > 60 km h^{-1} appears to be needed to trigger turbidity currents in Pointe-des-Monts, the latter were recorded 4-8 hours after the maximum wind speed (Figs. 6-7). There is thus a delayed response between maximum wind speed and the turbidity currents recorded by the ADCP.

The turbidity currents were also triggered during storm waves (Supplementary Table 2-3). The relationship is not so clear between wave height in Saint-Ulric or Rivière-Pentecôte and the four turbidity currents, since the fetches are different between these recording locations and Pointe-des-Monts (Fig. 8E-H). The two fastest turbidity currents on 25 January 2017 and 15 March 2017 were triggered during major storm waves from Northeast, when waves were highest in Saint-Ulric, but not the highest in Rivière-Pentecôte where the fetch from Northeast is more limited (Supplementary Table 2-3). Pointe-des-Monts is well exposed to Northeast waves but the South-facing canyon heads are protected (Fig. 1). During these storms, waves were likely breaking on the shallow rocky shelf, and wind and wave probably generated currents flowing southwestward, towards the canyon heads. The 4 January 2017 turbidity current was triggered with ENE wind when wave height was second highest in Rivière-Pentecôte (4.6 m) but wave heights were only 2 m in Saint-Ulric where the fetch is more limited from ENE. Again, the shelf of Pointe-des-Monts was exposed to these waves, but not the canyon heads. The 12 November 2017 turbidity current was triggered during strong Southwest wind, but the fetch is limited from this direction in Saint-Ulric (H_s barely above 2 m) and nearly null in Rivière-Pentecôte (Supplementary Table 2-3, Fig. 8E-H). However, Pointe-des-Monts must have been exposed to storm waves during this turbidity current event. To sum up, the four turbidity currents were triggered during high wave events, generally from Northeast. The relationship with duration of large wave height does not appear so strong, but the two fastest turbidity currents were triggered when wave heights > 3 m in Saint-Ulric lasted more than 5 hours.

Water column conditions prior to turbidity currents

In addition to being triggered during storms, all four turbidity currents were triggered at or near low tide. The low tides were not exceptional, but varied between 0.57 m (12/11/2016) and 2.12 m (15/03/2017) (Fig. 9). Comparing the tide during the turbidity current recorded by the ADCP to maximum wind speed recorded during the storms reveals that the combination of wind and tide is not exceptional for the four events compared to other periods of the year. Other periods experienced similar low tides and wind speed without triggering turbidity currents (Fig. 9A). A similar pattern is observed when comparing wave height in Saint-Ulric and Rivière-Pentecôte where wave height and tides do not appear to be significant on generating turbidity currents compared to other periods of the year (Fig. 9B-C).

On both 25 January and 15 March 2017, backscatter intensity increased 10 to 3 hours before the turbidity currents were recorded by the ADCP but during maximum wind speeds (Fig. 10C-D). These increases in backscatter intensity likely correspond to sediment plumes put in suspension during strong and sustained winds. These plumes were not observed on 12 November 2016 or 4 January 2017 (Fig. 10A-B), either because they did not occur or, more likely, because they occurred higher up in the canyon and were not recorded at the location of the ADCP.

The St-Lawrence Estuary was ice free around Pointe-des-Monts during three of the turbidity current events. Before the storm of 15 March 2017, the sea ice cover was 90% Northwest of Pointe-des-Monts and 70% to the South. The storm dispersed this partial ice cover, which nevertheless may have slightly reduced the size of the waves measured at St-Ulric and at Rivière-Pentecôte.

DISCUSSION

335 **What is the source of turbidity currents?**

336 Turbidity currents are nearly always triggered in locations where sediment supply from
337 rivers or longshore drift is important (Biscara et al., 2011; Ducassou et al., 2009;
338 Normandeau et al., 2016; Paull et al., 2011; Rogers & Goodbred, 2010). It is highly unusual
339 that a turbidite system remains active in the absence of sediment supply and with limited
340 volumes of sediment on the shelf. The Pointe-des-Monts shelf canyons are located 25 km
341 away from river inflow and have very limited supply by longshore drift, indicating that
342 turbidity currents are mostly remobilizing previously deposited deglacial and postglacial
343 sediment (Normandeau et al., 2014).

344 Turbidity currents can either be sourced from the shelf or from within the canyons
345 themselves. Bathymetric data show that there is limited volume of sediment available on
346 the shelf (Fig. 2). The rocky nature of the shelf with little sediment appears insufficient to
347 maintain the activity of turbidity currents (Normandeau et al., 2014). If they are triggered
348 from shelf remobilization, our results indicate that very little sediment is needed to generate
349 turbidity currents, especially on a very steep slope ($\geq 20°$) such as in Pointe-des-Monts.

350 Alternatively, the turbidity currents could originate from within the canyons rather than
351 from the shelf, most likely at a depth of > 100 m, where sediment offlaps the bedrock slope
352 (Fig 4A). For example, crescentic bedforms have migrated in the past decade within the
353 eastern gullies despite having their heads at 100 m water depth and the shelf above their
354 heads consisting mostly of bedrock (Fig. 4C).

355 **What triggered the turbidity currents?**

Normandeau et al. (2014) suggested that turbidity currents in Pointe-des-Monts could have been triggered by slope failures and/or hydrodynamic processes since no river mouths are located nearby (i.e., no hyperpycnal flows or other river-generated flows), but were unable to assess the precise timing of the events in the absence of direct monitoring. The five repeated bathymetric surveys carried out over the last decade clearly show that slope failures were limited to absent on the canyon walls and heads and were not responsible for triggering the turbidity currents leading to the migration of crescentic bedforms. Therefore, slope failures involving sediment thicker than 0.1 m of sediment (vertical resolution of the multibeam bathymetry in the upper reaches of the canyons) can conclusively be ruled out as the main trigger of turbidity currents down-canyon.

The data presented here indicates that the turbidity currents were triggered during storms. The common characteristic between the conditions that led to the four turbidity currents and that differentiate them from other storms is the continuous and sustained wind speed >60 km h^{-1}. For the two most intense turbidity currents, the wind blew from Northeast, and storm waves coming from Northeast were breaking on the shallow shelf. Another common characteristic is that they were triggered at or near low tide, but not extreme low water (Fig. 9). On deltas, low tides promote turbidity currents in association with high discharge because of increased sediment transport on the delta lip (Smith et al., 1990; Clare et al., 2016; Dietrich et al., 2016). Low tide can also promote slope failures because of change in pore pressures, promoting expansion of interstitial gas bubbles. Both cases require much more sediment on the shelf, which is not observed in Pointe-des-Monts (Fig. 2). Therefore, it is unclear if tides are important for the generation of turbidity currents or if their association with low tide is random. If such association exists, processes on the shallow

379 shelf would be involved in the turbidity current triggering because a 2-m lower water level
380 has much more impact in depth shallower than 10 m than in depth greater than 100 m.

381 The main question thus remains: How do the storms trigger the turbidity currents with
382 limited shelf sediment supply? Storms typically lead to wave-load excess pore pressure,
383 which can liquefy granular shelf sediment and induce failure (Puig et al., 2004). This
384 process can be ruled out since there is no evidence of large slope failures (> 0.1 m thick)
385 or of sufficient sediment on the shelf. Storms can also lead to off-shelf advection of
386 sediment (Piper & Normark, 2009) where low tide could allow storm waves to more
387 effectively suspend sediment on the shelf due to greater wave influence. This mechanism
388 would appear more likely here even though the volume of sediment on the shelf is limited.
389 Nonetheless, the Northeast wind could generate currents and waves that resuspended
390 limited volumes of sediment on the shelf that flow over a steep slopes and that generate
391 turbidity currents (Fig. 12A). This mechanism has been observed in San Lucas Canyon,
392 offshore Baja California where underwater sand falls flowing down-canyon were
393 photographed while diving (Shepard and Dill, 1966, their Fig. 55). This process might be
394 similar to what occurs in Pointe-des-Monts if the turbidity currents are indeed triggered
395 from the shelf.

396 Unlike Normandeau et al. (2014) previously suggested, no specific hydrodynamic
397 processes (e.g., internal waves, internal tides) were observed during or prior to the turbidity
398 currents. However, such processes could have occurred in the upper water column and not
399 have been recorded by the downward-looking ADCP. For example, wind stress
400 fluctuations can generate internal waves (D'Asaro, 1984), which could then suspend
401 sediment and trigger turbidity currents when shoaling on the upper slope (Fig. 12A).

During the two most important turbidity currents, shelf or canyon head sediment resuspension is interpreted from high backscatter in the water column between 165 m and 185 m water depth (ADCP measurements), 4 to 10 hours prior to turbidity currents (Fig. 10C-D). This inferred sediment resuspension suggests that a mechanism associated with sustained and strong wind speed generated enough shear stress for the suspension of sediment and its advection offshore. Regardless of whether the sediment were resuspended on the shelf or within the canyon heads, when the suspended sediment concentration reached a threshold, turbidity currents could have been triggered, most likely in a similar manner as the settling of sediment plumes on river deltas (Hizzett et al., 2017)(Fig. 12A). Inman et al. (1976) also suggested that pile-up of water on the shelf caused by strong winds and down-canyon pulses of currents and water caused by surface waves could lead to sustained down-canyon currents (turbidity currents). Our study cannot provide evidence for this mechanism occurring since the ADCP was located in 165 m water depth. Therefore, pulses of water piling on the shelf or pulses of currents could not be recorded since these processes occur near the shelf-edge rather than in deeper waters. Nonetheless, although we cannot point out the exact mechanism by which storms trigger turbidity currents in Pointe-des-Monts, this study provides evidence for turbidity currents triggered by sediment suspension during storms instead of liquefaction of sediment by wave load excess pore pressure. This general mechanism is more clearly expressed by the eastern gullies that offlap bedrock and from which upslope liquefaction of sediment during storms is unlikely (Fig. 4). On the other hand, small patches of sediment are observed in the main canyon heads (Fig. 2), which could lead to occasional thin-skinned surficial failures in that part of the system. However, mapping of the shelf in 2012 did not reveal the presence of large area

425 of thin-skin failure, which suggest that this mechanism is unlikely to be prevalent, although
426 it could contribute to occasional turbidity currents.

427 **Dense basal layers and the rapid upslope migration of bedforms**

428 Although four turbidity currents were triggered during the winter of 2016-2017, they did
429 not have a similar effect on the seafloor. Turbidity currents triggered on 12 November 2016
430 and on 4 January 2017 were slow moving (< 0.5 m s^{-1}) and either by-passed the location
431 of the ADCP or deposited very little sediment (< 1 cm) which could not be resolved by the
432 ADCP. Therefore, these small and weak turbidity currents had very little effect on the
433 seafloor and did not lead to the migration of the bedforms. They appeared similar to some
434 of the small and dilute turbidity currents recorded in Monterey Canyon (Xu et al., 2013)
435 and Squamish delta (Hughes Clarke et al., 2014) because they are slow and have had no
436 discernable effect on the seafloor.

437 On 25 January 2017, a slightly stronger turbidity current occurred with a faster flowing
438 front (0.55 m s^{-1}). This event produced a lasting change on the seafloor since the distance
439 of the seafloor from the ADCP was shallower following this event, indicating that ~0.1 m
440 of sediment was deposited (Fig. 11G). 360° depth profiles with a diameter of 16 m around
441 the ADCP before and after the event suggest that sediment was deposited on the stoss side
442 of a bedform and slight erosion occurred on the lee side (Fig. 11D). Similar observations
443 of upslope migrating bedforms have been associated to cyclic steps instabilities (Hughes
444 Clarke, 2016; Hage et al., 2018), which occur at the base of supercritical flows (Postma
445 and Cartigny, 2014; Hughes Clarke, 2016). Therefore, the upslope migration of the
446 crescentic bedforms appear to be related to an upper flow regime and to represent cyclic
447 step bedforms (e.g., Fildani et al., 2006). Although this event appears to have led to minor

upslope migration of crescentic bedforms, it was not responsible for the ~7 m of upslope migration at the location of the mooring recorded from repeat bathymetric surveys.

The most intense turbidity current by far occurred on 15 March 2017, with speeds reaching up to 2.2 m s^{-1}. During this storm-related event, the seafloor-ADCP distance became shorter by 0.4 m. Concomitantly, the depth of the ADCP itself became abruptly shallower by ~0.3 m. Correlating the 360° depth profile of the ADCP to the multibeam data reveals that the mooring was displaced down-canyon ~10 m toward ENE (60° direction; Fig. 11), which corresponds to the direction of turbidity current pulse 2A (Fig. 6B). The mooring was rapidly displaced within 1 minute of the 70 minute-long event. Since the ADCP became shallower, it indicates that it was displaced up the stoss side of a bedform. During the displacement of the mooring, the roll and tilt of the ADCP did not exceed 2.1°. Although the tilting was rapid at turbidity current arrival, the values recorded are not greater than other moments where turbidity currents were not present. This suggest that drag on the mooring is unlikely to be responsible for the displacement of the mooring since tilting would have been greater than other times dominated by tidal currents. Therefore, the low tilting values, in combination with the rapid displacement of the 300 kg mooring up the stoss side of a bedform probably indicates that the lower part of the flow was responsible for the mooring displacement. In other systems, such as Monterey and Squamish, such displacement of heavy objects were explained by the presence of dense basal layers that drive the flows (e.g., Hughes Clarke, 2016; Paull et al., 2018). The results presented here support the presence of such a dense basal layer in turbidity currents that appear to drive the early part of turbidity currents. If it was present, it is unclear if the dense basal layer lasted more than 1 minute since no movement of the mooring was recorded

following pulse 2A. However, dense basal layers were hypothesized to either wipe out pre-existing bedforms and creating new bedforms or to simply modify pre-existing bedforms (Paull et al., 2018). Our repeat bathymetric data clearly shows that pre-existing bedforms were not wiped out by the turbidity current and that bedforms were modified by the dense basal front of the turbidity current.

The shorter ADCP-seafloor distance indicates that the mooring anchor (200-kg train wheel) was buried under ~0.4 m of sediment (Fig. 11E). The 360° depth profile from the ADCP is well correlated with the 2016 multibeam data until the very last minutes preceding this event (Fig. 11F), indicating that little seabed change occurred before that date. At this location and time (before the 15 March event), the 360° depth profile is uncorrelated with the 2017 multibeam data (Fig. 11F), both because the seabed has changed and the mooring was displaced. When the mooring is re-positioned accordingly on the map, the 360° depth profile from the ADCP after the event correlates with the 2017 multibeam data (Fig. 11H), already two hours after the 15 March 2017 event. This indicates that most of the major irreversible seabed change observed between the 2016 and 2017 multibeam data occurred rapidly, in less than two hours and that it was caused by the turbidity current of 15 March 2017. This event is thus responsible for the up to 7 m of lee-side erosion recorded near the mooring location and occurred under 1 minute of the ~70 minute flow. These data indicate that although turbidity currents can be long-lasting (i.e., 70 minutes in this case), only the fast flowing front leads to significant change on the seabed, likely driven by a dense basal layer.

Behaviour of storm-induced turbidity currents and the role of flow ignition

493 The combination of repeat multibeam bathymetry and ADCP measurements allows us to
494 illustrate the behaviour and structure of storm-induced turbidity currents responsible for
495 the upslope migration of crescentic bedforms. The upper region of the main canyon is the
496 most active part of the system, with a minimum of one turbidity current every three years.
497 However, this estimate is based on events that led to the migration of crescentic bedforms.
498 It is more likely that the frequency of events is higher since frequent small flows may not
499 be eroding the seafloor and, therefore, not be recorded in the bathymetry data.

500 In the upper reaches of the canyon, the slope is locally steep (>15°), which triggers turbidity
501 currents when suspended sediment concentration is sufficient. The steepness of the upper
502 slope suggests that the turbidity currents traveling downslope should be supercritical. The
503 presence of upslope migrating crescentic bedforms strongly suggests that these bedforms
504 are formed by periodic hydraulic jumps, where flows are supercritical on the lee-side of
505 the bedform and subcritical on the stoss side of the bedforms (Kostic, 2011). Therefore, as
506 suggested by the ADCP and repeat bathymetry data, the crescentic bedforms are most
507 likely cyclic steps (Parker 1996).

508 When the turbidity currents flow over the lee side of these cyclic steps, the erosion of
509 sediment may lead to flow ignition (Fig. 12B), a process by which the increased sediment
510 concentration, and thus density, increases the velocity of the flow (Parker, 1982). Flow
511 ignition, also called flow self-acceleration, requires turbidity currents to be supercritical
512 (Pantin and Franklin, 2009). The presence of cyclic steps in the canyon system indicates
513 that the flows are indeed supercritical and are thus prone to self-acceleration. Additionally,
514 flow dynamics is known to be very sensitive to changes in sediment or water entrainment
515 (Traer et al., 2012). Small changes in sediment concentration can lead to self-acceleration.

Sequeiros et al. (2018) have shown that slope gradient and the initial discharge were important for self-acceleration to occur. In Pointe-des-Monts, the higher initial discharge resulting from storm sediment resuspension (Fig. 10) might explain why currents on 25 January and 15 March were faster and more erosive than the other ones. The higher discharge increases flow velocity (Sequeiros et al., 2018), which in turn increases erosion in the steep upper reaches of the canyons. In these sectors, very little deposition is observed compared to erosion, suggesting that flows incorporate sediment while travelling downslope, which may then be responsible for igniting them. We thus suggest that erosion of lee-side slopes may be an important factor in igniting storm-induced turbidity currents considering the limited volume of sediment that is present in the upper reaches of the system and shelf (Fig. 12B).

In the main canyon, the four upper reaches have relatively similar migration rates, with the exception of the eastern one (Fig. 3). Where those four reaches merge, migration rates are the largest, indicating that currents are strongest, leading to more lee-side erosion. In fact, within the narrow part of the canyon where flows merge, bedforms migrated upslope by more than a half-wavelength, giving the appearance of downslope migration between surveys (Fig. 3B). Flows accelerate in that narrow reach, thereby increasing upslope migration rates. Farther downslope, the channel width then increases from 60 m to more than 160 m, which leads to flow dissipation, as similarly observed on the Squamish delta (e.g., Stacey et al., 2018). No change on the seafloor is observed downslope on the lobe. When flows slow down slightly, sediment deposition and water entrainment lead to reduced sediment concentration, which then reduces the speed of the turbidity current, thereby leading to more deposition (e.g., Stacey et al., 2018). Similar flow unconfinement

539 is observed in the eastern gullies where bedforms migrate within the gullies, but not on the
540 lobes. Therefore, although flows likely ignite in the confined regions of the canyons, when
541 they become unconfined water entrainment reduces sediment concentration, thereby
542 reducing the erosive nature of the turbidity currents. This process appears to occur rapidly
543 upon channel unconfinement since the bedforms rather abruptly stop migrating.

544 In the middle canyon, one or more turbidity currents had an effect on the seafloor down to
545 the lobe. The middle canyon is more confined throughout its course and down to the lobe
546 downslope. Flow confinement is thus critical for these types of turbidity currents to
547 generate frequent migration of cyclic steps. As soon as flows dissipate, rates of migration
548 are either null or very low over decades.

549 **Types of turbidity currents shaping the seafloor**

550 Recent studies have shown that turbidity currents in submarine canyons are bi-modal,
551 classified as canyon-filling and canyon-flushing events (Allin et al., 2016; Jobe et al.,
552 2018). According to the effect of turbidity currents on the seafloor (i.e., bedform
553 migration), this study shows that flows are also bi-modal in the Pointe-des-Monts turbidite
554 system (Fig. 12A). The first type of flow is weak ($\leq$0.3 ms^{-1}) in that it does not lead to the
555 migration of bedforms and leaves no discernable deposit through repeated bathymetry or
556 ADCP measurements. This type of flow cannot be recorded without the use of water
557 column measurements (ADCP). It likely cannot be recorded in the sedimentary record
558 since it would be remobilized by the second type of flow, which is much more erosive. The
559 second type of turbidity currents leads to the migration of bedforms in the upper reaches
560 of canyons and channels and is illustrated by the 25 January and 15 March 2017 events.
561 These events lead to the migration of bedforms when confined in channels, but as soon as

562 they dissipate, flows have little to no effect on the seafloor. However, it could be that the
563 sediment waves on the lobe migrate at a very slow rate, not discernable to the repeat
564 bathymetry. These flows likely form the bulk (i.e., the main component) of the sedimentary
565 record. Another option is that even larger flows, which were not observed during our
566 mooring period are responsible for the migration of sediment waves down on the lobes.
567 These flows would be powerful enough to have an effect on the seafloor even when
568 unconfined. If these flows occur, they appear to be rare, as they were not observed during
569 our decade-long mapping study.

570 **Implications for the activity of submarine canyons worldwide and the role of shelf**
571 **width and depth**

572 This study shows that coasts and shelves with limited volume of sediment, where turbidity
573 currents would not be expected to be active because of the rocky shoreline, can also be
574 locations where turbidity currents are occurring. Most (if not all) studies monitoring
575 turbidity currents have been in places where sediment supply from a river or from
576 longshore drift is high. For example, the best known examples of active turbidity currents
577 are on North America's West Coast, on deltas with high sediment supply (e.g., Prior et al.,
578 1987; Lintern et al. 2016; Hughes Clarke, 2016) or at the end of a littoral cell composed of
579 large sandy beaches (e.g., Inman et al., 1976; Paull et al., 2005; Covault & Fildani, 2014)
580 (Fig. 13). It is thus rather unexpected that the Pointe-des-Monts canyons are active where
581 the shoreline consists mostly of bedrock and small isolated beaches (Normandeau et al.,
582 2014). The main reason that could explain why they are active is that similarly to longshore
583 drift-fed submarine canyons, they are located very close to the shoreline and their heads
584 are in shallow water (Fig. 13). Even though sediment supply is limited, this connection

appears critical in submarine canyons activity (e.g., Paull et al., 2005; Sweet and Blum 2016). In this scenario, surface waves and wind processes can actively interact with canyon heads and remobilize small volumes of sediments into canyon heads. Regardless of sediment supply, if canyon heads interact with the shallow shelf or shoreline and the slope is steep enough, the likelihood of turbidity currents being triggered is higher, probably higher than submarine canyons with sediment are their heads, but that are too deep to interact with surface processes such as winds and waves. Therefore, it is worthwhile examining shore-connected submarine canyons located in sediment-starved regions in order to precise the minimum requirements (e.g., sediment supply, tectonic setting, oceanographic processes, etc.) for turbidity currents to be triggered. This is particularly important for geohazards assessment.

The comparison of the Pointe-des-Monts canyons with other canyons also highlights the predominant role storms play in triggering turbidity currents. In other systems such as Monterey and Squamish, some turbidity currents had no apparent triggers (Hughes Clarke et al., 2014, Paull et al., 2018) whereas in Pointe-des-Monts, all four turbidity currents were clearly related to storms. This difference is likely related to sediment supply where supply-dominated canyons respond differently to external triggers than sediment-starved canyons. For example, sediment supply can over steepen a slope during fairwater conditions and generate slope failures, which in turn stabilizes the slope in the event of a storm the following days or weeks. These processes are unlikely to occur in sediment-starved margins, which makes the external triggers more likely to lead to turbidity currents than in supply-dominated margins.

CONCLUSIONS

608 The Pointe-des-Monts shelf canyons represent a peculiar system in that they are active
609 although limited in sediment supply on the shelf. A decade-long monitoring program
610 including repeat high-resolution seafloor bathymetry and a 2-year direct monitoring
611 program revealed the timing of turbidity currents and their direct effect on the upslope
612 migration of crescentic bedforms. The following conclusions can be drawn from the
613 analysis of these datasets:

614 1) The turbidity currents are triggered during sustained high wind speed (> 60 km h^{-1}),
615 during large storms and storm waves;
616 2) The source of sediment for the turbidity currents does not appear to involve the
617 failure of canyon or channel-wall. Rather, the data suggest that limited volumes of
618 sediment resuspended on the shelf or the canyon head (100 m deep) are sufficient
619 to trigger turbidity currents during storms. A suspended sediment concentration
620 threshold is then reached for a turbidity current to form. Then, by eroding sediment
621 in the upper reaches of the system, flows ignite and allow them to travel greater
622 distances downslope and shape the entire canyon until unconfined. Flow ignition
623 thus appears to be an important process in turbidite systems with limited volume of
624 sediment supply from the shelf;
625 3) The fast flowing front of the more intense turbidity currents are responsible for the
626 upslope migration of bedforms. This fast flowing front was responsible for
627 displacing the 200 kg mooring by 10 m up the stoss side of a crescentic bedforms,
628 interpreted as a cyclic step, in less than 1 minute, while the entire turbidity current
629 lasted about 70 minutes. Similarly to other locations, turbidity currents in Pointe-
630 des-Monts can displace a heavy mooring down-canyon, and upslope on the stoss

631 side of a bedform, suggesting that dense basal layers are driving the early fast
632 moving parts of the turbidity currents. This very rapid migration of the mooring
633 and crescentic bedforms indicates that only the front of turbidity currents are dense
634 and powerful enough to generate upslope migrating bedforms in a very short period
635 of time. The dense basal layer also appears to modify pre-existing bedforms rather
636 than wiping them out and creating new ones and is therefore responsible for the
637 higher rates of bedform migration.

638 4) Upcanyon migration of bedforms occurs in confined channels, indicating that flow
639 unconfinement leads to flow dissipation, which is then unable to generate the
640 migration of bedforms or other significant change on the seafloor;

641 5) The combination of multibeam bathymetry mapping with direct monitoring using
642 an ADCP reveals that two main types of turbidity currents with different intensities
643 occur in the Pointe-des-Monts system: 1) weak turbidity currents with negligible
644 effect on the seafloor; 2) intense turbidity currents which leads to the migration of
645 bedforms in confined stretches.

646 These results stress the fact that a complete understanding of turbidity current triggers and
647 canyon morphodynamics from a combined direct monitoring and repeat seabed mapping
648 study should be the focus of upcoming studies. Identifying the exact triggers of turbidity
649 currents and their precise effect on the seafloor are critical for risk reduction associated
650 with submarine infrastructure. These processes might also be more prevalent than currently
651 known since they can be triggered on sediment starved shelves where submarine canyon
652 heads are located in shallow water and where hydrodynamics and oceanographic factors
653 control the triggering of turbidity currents.

ACKNOWLEDGEMENTS

This study was supported by the Natural Sciences and Engineering Research Council of Canada through Discovery and Ship-time grants to P.L., G.S., D.B. The captain and crew of the R/V Coriolis are thanked for their help during the deployment and recovery of the moorings. Gilles Desmeules is particularly thanked for these operations. CIDCO is thanked for part of the multibeam data acquisition. Louis Gostiaux was partially funded by the ANR-13-JS09-0004-01 (STRATIMIX). The wave recording was supported by the 2013-2020 Climate Change Action Plan of the Government of Québec and its Green Fund. We thank Matthieu Cartigny, Mike Clare and Andrea Fildani for their comments that greatly improved the quality of this manuscript. The data that support the findings of this study are available from the corresponding author upon reasonable request.

REFERENCES

Allin, J. R., Hunt, J. E., Talling, P. J., Clare, M. A., Pope, E., and **Masson, D. G.** (2016) Different frequencies and triggers of canyon filling and flushing events in Nazaré Canyon, offshore Portugal. *Marine Geology*, **371**, 89–105.

Ayranci, K., Lintern, D. G., Hill, P. R., and **Dashtgard, S. E.** (2012) Tide-supported gravity flows on the upper delta front, Fraser River delta, Canada. *Marine Geology*, **326,** 166-170.

Azpiroz-Zabala, M., Cartigny, M. J., Talling, P. J., Parsons, D. R., Sumner, E. J., Clare, M. A., **Simmons, S.M., Cooper, C.** and **Pope, E. L.** (2017a). Newly recognized turbidity current structure can explain prolonged flushing of submarine canyons. *Science advances*, **3**, e1700200.

Azpiroz-Zabala, M., Cartigny, M. J. B., Sumner, E. J., Clare, M. A., Talling, P. J., Parsons, D. R., and **Cooper, C.** (2017b) A General Model for the Helical Structure of Geophysical Flows in Channel Bends. *Geophysical Research Letters*, **44**, 11 932-11 941.

Biscara, L., Mulder, T., Martinez, P., Baudin, F., Etcheber, H., Jouanneau, J.-M., and **Garlan, T.** (2011) Transport of terrestrial organic matter in the Ogooué deep sea turbidite system (Gabon). *Marine and Petroleum Geology*, **28**, 1061–1072.

Bornhold, B.D., Ren, P., Prior, D.B. (1994) High-frequency turbidity currents in British Columbia fjords. *Geo-Marine Letter*s **14**, 238-243.

Bourgault, D., Mosilli, C., Richards, C., Neumeier, U. and Kelley, D. (2014) Sediment resuspension and nepheloid layers induced by long internal solitary waves shoaling orthogonally on uniform slopes. *Continental Shelf Research* **72**, 21-33.

Bruschi, R., Bughi, S., Spinazzè, M., Torselletti, E. and Vitali, L. (2006) Impact of debris flows and turbidity currents on seafloor structures. *Norwegian Journal of Geology/Norsk Geologisk Forening***, 86**.

Carter, L., Gavey, R., Talling, P. J., and **Liu, J. T.** (2014) Insights into submarine geohazards from breaks in subsea telecommunication cables. *Oceanography*, **27**, 58-67.

Clare, M. A., Hughes Clarke, J. E., Talling, P. J., Cartigny, M. J. B., and **Pratomo, D. G.** (2016) Preconditioning and triggering of offshore slope failures and turbidity currents revealed by most detailed monitoring yet at a fjord-head delta. *Earth and Planetary Science Letters*, **450**, 208–220.

Conway, K.W., Kung, R.B., Barrie, J.V., Hill, P.R. and Lintern, D.G. (2013) A preliminary assessment of the occurrence of submarine slope failures in coastal British

Columbia by analysis of swath multibeam bathymetric data collected 2001-2011. *Geological Survey of Canada Open File,* **3748**, 38 p.

Cooper, C., Wood, J., and **Andrieux, O.** (2013) Turbidity current measurements in the Congo Canyon. In *Proceedings of Offshore Technology Conference* (pp. 1–4).

Covault, J.A. and Fildani, A. (2014) Continental shelves as sediment capacitors or conveyors: Source-to-sink insights from the tectonically active Oceanside shelf, southern California, USA. *Geological Society of London Memoir*, **41**, 315-326.

Covault, J. A., Kostic, S., Paull, C. K., Sylvester, Z., and **Fildani, A.** (2017). Cyclic steps and related supercritical bedforms: building blocks of deep-water depositional systems, western North America. *Marine Geology*, **393**, 4-20.

D'Asaro, E. A. (1984) Wind forced internal waves in the North Pacific and Sargasso Sea. *Journal of Physical Oceanography*, **14**, 781–794.

Dietrich, P., Ghienne, J.-F., Normandeau, A., and **Lajeunesse, P.** (2016) Upslope-Migrating Bedforms In A Proglacial Sandur Delta: Cyclic Steps From River-Derived Underflows? *Journal of Sedimentary Research*, **86**, 113–123.

Dietrich, P., Ghienne, J. F., Schuster, M., Lajeunesse, P., Nutz, A., Deschamps, R., Roquin, C. and **Duringer, P.** (2017) From outwash to coastal systems in the Portneuf–Forestville deltaic complex (Québec North Shore): Anatomy of a forced regressive deglacial sequence. *Sedimentology*, **64**, 1044–1078.

Ducassou, E., Migeon, S., Mulder, T., Murat, A., Capotondi, L., Bernasconi, S. M., and **Mascle, J.** (2009) Evolution of the Nile deep-sea turbidite system during the Late Quaternary: influence of climate change on fan sedimentation. *Sedimentology*, **56**, 2061–

2090.

Fildani, A., Normark, W.R., Kostic, S. and Parker, G. (2006) Channel formation by flow stripping: large-scale scour features along the Monterey East Channel and their relation to sediment waves. *Sedimentology*, **53**, 1265–1287

Heezen, B. C., and **Ewing, M.** (1952) Turbidity currents and submarine slumps, and the 1929 Grand Banks earthquake. *American journal of Science*, **250**, 849-873.

Hage, S., Cartigny, M. J., Clare, M. A., Sumner, E. J., Vendettuoli, D., Hughes Clarke, J. E., Hubbard, S.M., Talling, P.J., Lintern, G.., Stacey, C.D., Englert, R. G., Vardy, M.E., Hunt, J.E., Yokokawa, M., Parsons, D.R., Hizzett, J.L., Azpiroz-Zabala, M. and **Vellinga, A.J.** (2018) How to recognize crescentic bedforms formed by supercritical turbidity currents in the geologic record: Insights from active submarine channels. *Geology*, **46**, 563-566.

Hizzett, J. L., Hughes Clarke, J. E., Sumner, E. J., Cartigny, M. J. B., Talling, P. J., and **Clare, M. A.** (2017) Which triggers produce the most erosive, frequent and longest runout turbidity currents on deltas? *Geophysical Research Letters*, **45**, 855–863.

Hughes Clarke, J. E. (2016) First wide-angle view of channelized turbidity currents links migrating cyclic steps to flow characteristics. *Nature Communications*, **7**, 11896.

Hughes Clarke, J., Vidiera Marques, C. R., and **Pratomo, D.** (2014) Imaging Active Mass-Wasting and Sediment Flows on a Fjord Delta, Squamish, British Columbia. In S. Krastel, J.-H. Behrmann, D. Völker, M. Stipp, C. Berndt, R. Urgeles, … C. B. Harbitz (Eds.), *Submarine Mass Movements and Their Consequences, Advances in Natural and Technological Hazards Research*, **37**, 249–260. Springer.

Inman, D.L., Nordstrom, C.E., Flick, R.E. (1976) Currents in submarine canyons: An air-sea-land interaction. Annual Review of Fluid mechanics, **8**, 275-310.

Jobe, Z. R., Howes, N., Romans, B. W., and **Covault, J. A.** (2018) Volume and recurrence of submarine-fan-building turbidity currents. *The Depositional Record*, **4**. 160-176.

Khripounoff, A., Vangriesheim, A., Babonneau, N., Crassous, P., Dennielou, B., and **Savoye, B.** (2003) Direct observation of intense turbidity current activity in the Zaire submarine valley at 4000 m water depth. *Marine Geology*, **194**, 151–158.

Kostic., S. (2011) Modeling of submarine cyclic steps: Controls on their formation, migration, and architecture. *Geosphere*, **7**, 294-304

Koutitonsky, V.G., Bugden, G.L., (1991) The physical oceanography of the Gulf of St. Law- rence: a review with emphasis on the synoptic variability of the motion. In: Therriault, J.-C. (Ed.), The Gulf of St. Lawrence: small ocean or large estuary?. *Canadian Special Publication of Fisheries and Aquatic Science*. **113**, 57–90.

Lintern, D. G., Hill, P. R., and **Stacey, C.** (2016) Powerful unconfined turbidity current captured by cabled observatory on the Fraser River delta slope, British Columbia, Canada. *Sedimentology*, **63**, 1041-1064.

Normandeau, A., Dietrich, P., Lajeunesse, P., St-onge, G., Ghienne, J., Duchesne, M. J., and **Francus, P.** (2017) Timing and controls on the delivery of coarse sediment to deltas and submarine fans on a formerly glaciated coast and shelf. *GSA Bulletin*, **129**, 1424–1441.

Normandeau, A., Lajeunesse, P., Poiré, A. G., and **Francus, P.** (2016) Morphological

764 expression of bedforms formed by supercritical sediment density flows on four fjord-lake
765 deltas of the south-eastern Canadian Shield (Eastern Canada). *Sedimentology*, **63**, 2106–
766 2129.

767 **Normandeau, A., Lajeunesse, P.,** and **St-Onge, G.** (2015) Submarine canyons and
768 channels in the Lower St. Lawrence Estuary (Eastern Canada): Morphology, classification
769 and recent sediment dynamics. *Geomorphology*, **241**, 1–18.

770 **Normandeau, A., Lajeunesse, P., St-Onge, G., Bourgault, D., Drouin, S. S. O.,**
771 **Senneville, S.,** and **Bélanger, S.** (2014) Morphodynamics in sediment-starved inner-shelf
772 submarine canyons (Lower St. Lawrence Estuary, Eastern Canada). *Marine Geology*, **357**,
773 243–255.

774 **Pantin, H. M., and Franklin, M. C.** (2009). Predicting autosuspension in steady
775 turbidity flow: Ignition points and their relation to Richardson numbers. *Journal of*
776 *Sedimentary Research*, **79** , 862–871.

777 **Parker, G.** (1982) Conditions for the ignition of catastrophically erosive turbidity currents.
778 *Marine Geology*, **46**, 307–327.

779 **Parker, G.** (1996) Some speculations on the relation between channel morphology and
780 channel-scale flow structures. In: *Coherent Flow Structures in Open Channels* (Ed. P.
781 Ashworth, S. Bennett, J. Best and S. McLelland), pp. 423–458. John Wiley & Sons, New
782 York

783 **Paull, C.K., Ussler, W., Greene, H.G., Keaten, R., Mitts, P., Barry, J.** (2003) Caught in
784 the act: the 20 December 2001 gravity flow event in Montery Canyon. *Geo-Marine Letters*,
785 **22**, 227-232.

Paull, C.K., Mitts, P., Ussler III, W., Keaten, R. and Greene, H.G. (2005) Trail of sand in upper Montery Canyon: Offshore California. *GSA Bulletin*, **117**, 1134-1145.

Paull, C. K., Caress, D. W., Ussler III, W., Lundsten, E., and **Meiner-Johnson, M.** (2011) High-resolution bathymetry of the axial channels within Monterey and Soquel submarine canyons, offshore central California. *Geosphere*, **7**, 1077–1101.

Paull, C.K., Talling, P. J., Maier, K. L., Parsons, D., Xu, J., Caress, D. W., Gwiazda, R., Lundsten, E.M., Anderson, K., Barry, J.P., Chaffey, M., O'Reilley, T., Rosenberger, K.J., Gales, J.A., Kieft, B., McGann, M., Simmons, S.M., McCann, M., Sumner, E.J., Clare, M.A., and **Cartigny, M.J.** (2018) Powerful turbidity currents driven by dense basal layers. *Nature communications*, **9**, 4114.

Pawlowicz, R., Beardsley, B., and **Lentz, S.** (2002) Classical tidal harmonic analysis including error estimates in MATLAB using t_tide. *Computers and Geosciences*, **28**, 929-937.

Pinet, N., Brake, V., Campbell, C., and **Duchesne, M. J**. (2015) Geomorphological characteristics and variability of Holocene mass-transport complexes, St. Lawrence River Estuary, Canada. *Geomorphology*, **228**, 286–302.

Piper, D. J. W., and **Normark, W. R.** (2009) Processes That Initiate Turbidity Currents and Their Influence on Turbidites: A Marine Geology Perspective. *Journal of Sedimentary Research*, **79**, 347–362.

Postma, G., Cartigny, M.J.B. (2014) Supercritical and subcritical turbidity currents and their deposits – A synthesis. *Geology*, **42**, 987-990.

Prior, D.B., Bornhold, B.D., Wiseman Jr, W.J., Lowe, D.R. (1987) Turbidity current

activity in a British Columbia Fjord*, Science*, **237**, 1330-1333.

Puig, P., Ogston, A. S., Mullenbach, B., Nittrouer, C. A., Parsons, J. D., and **Sternberg, R. W.** (2004) Storm-induced sediment gravity flows at the head of the Eel submarine canyon, northern California margin. *Journal of Geophysical Research*, **109**.

Puig, P., Palanques, A., Guillén, J., and **El Khatab, M.** (2004) Role of internal waves in the generation of nepheloid layers on the northwestern Alboran slope: Implications for continental margin shaping. *Journal of Geophysical Research C: Oceans*, **109**, 1–11.

Puig, P., Palanques, A., Orange, D. L., Lastras, G., and **Canals, M.** (2008). Dense shelf water cascades and sedimentary furrow formation in the Cap de Creus Canyon, northwestern Mediterranean Sea. *Continental Shelf Research*, **28**, 2017–2030.

Puig, P., Palanques, A., and **Martín, J.** (2014) Contemporary sediment-transport processes in submarine canyons. *Annual review of marine science*, **6**, 53-77.

Rogers, K. G., and **Goodbred, S. L.** (2010) Mass failures associated with the passage of a large tropical cyclone over the Swatch of No Ground submarine canyon (Bay of Bengal). *Geology*, **38**, 1051–1054.

Saucier, F.J., Roy, F., Gilbert, D., Pellerin, P., Ritchie, H., (2003) Modeling the formation and circulation processes of water masses and sea ice in the Gulf of St. Lawrence, Canada. *Journal of Geophysical Research* **108**, 1–20.

Sequeiros, O. E., Mosquera, R. L., and Pedocchi, F. (2018). Internal structure of a self-accelerating turbidity current. *Journal of Geophysical Research: Oceans*, **123**, 6260–6276

Sheppard, F.P. and Dill, R.F. (1966) Submarine canyons and other sea valleys. Rand McNally & Company, Chicago, 381 p.

Shepard, F.P., Marshall, N.F. (1973) Storm-generated current in La Jolla Submarine Canyon, California. *Marine Geology*, **15**, 19-24.

Smith, N., Phillips, A., and Powell, R. (1990) Tidal drawdown: A mechanism for producing cyclic sediment laminations in glaciomarine deltas. *Geology*, **18**, 1-10.

Stacey, C. D., Hill, P. R., Talling, P. J., Enkin, R. J., Hughes-Clarke, J. E., and **Lintern, D. G.** (2018) How turbidity current frequency and character varies down a fjord-delta system: Combining direct monitoring, deposits and seismic data. Sedimentology.

Sumner, E. J., and **Paull, C. K.** (2014) Swept away by a turbidity current in Mendocino submarine canyon, California. *Geophysical Research Letters*, **41**, 7611-7618.

Sweet, M.L. and Blum, M.D. (2016) Connections between fluvial to shallow marine environments and submarine canyons: Implications for sediment transfer to deep water. *Journal of Sedimentary Research*, **86**, 1147-1162.

Traer, M. M., G. E. Hilley, A. Fildani, and T. McHargue (2012), The sensitivity of turbidity currents to mass and momentum exchanges between these underflows and their surroundings, Journal of Geophysical Research., **117**, F01009.

Xu, J. P., Barry, J. P., and **Paull, C. K.** (2012) Small-scale turbidity currents in a big submarine canyon. *Geology*, **41**, 143–146.

Xu, J. P., Sequeiros, O. E., and **Noble, M. A.** (2014) Sediment concentrations, flow conditions, and downstream evolution of two turbidity currents, Monterey Canyon, USA.

Deep Sea Research Part I: Oceanographic Research Papers, **89**, 11–34.

Zeng, J., Lowe, D.R., Prior, D.B., Wiseman Jr, W.J., Bornhold, B.D. (1991) Flow properties of turbidity currents in Bute Inlet, British Columbia. *Sedimentology*, **38**, 975-996.

Zhang, Y., Liu, Z., Zhao, Y., Colin, C., Zhang, X., Wang, M., Zhao, S. and **Kneller, B.** (2018) Long-term in situ observations on typhoon-triggered turbidity currents in the deep sea. *Geology*.

858 **Figures and tables**

859

860 **Figure 1**. A) Location of the Pointe-des-Monts turbidite system, Lower St. Lawrence
861 Estuary (eastern Canada). B) Multibeam bathymetry (2012) of the Pointe-des-Monts
862 canyon system with location of moorings 1 (M1, 2015-2016) and 2 (M2, 2016-2017). C)
863 Timeline of the Pointe-des-Monts moorings and bathymetric surveys, including dates of
864 multibeam surveys where bedform migration was observed and ADCP mooring with
865 timing of turbidity currents recorded. D) Design of the second mooring deployed in Pointe-
866 des-Monts that recorded turbidity currents.

867 **Figure 2**. Coastal (satellite imagery) and nearshore geomorphology (bathymetry)
868 illustrating the limited volume of sediment on the shelf and coast. Note the location of
869 bedrock outcrops. Location provided in Figure 1.

870 **Figure 3**. Difference maps of the Pointe-des-Monts canyons: A) 2017-2012 difference
871 map illustrating the upslope migration of crescent-shaped bedforms in all canyons and
872 gullies; B) 2015-2012 difference map of the main canyon illustrating the lee side erosion
873 and stoss side deposition responsible for the upslope migration of bedforms; C) 2017-2016
874 difference map revealing migration of bedforms during mooring 2.

875 **Figure 4**. A) Multibeam bathymetry image of the eastern gullies illustrating the
876 unconsolidated post-glacial sediment on bedrock; 2) 2015-2012 difference map illustrating
877 the migration of bedforms in the gullies despite no evidence of slope failures during the
878 two years (see Fig. 2); C) 3D perspective of the eastern gullies offlapping the bedrock
879 slope.

880 **Figure 5**. Atmospheric and water column measurements for the entire mooring 2 period
881 (12 October 2016 to 12 October 2017) with four turbidity current events (shaded area): A)
882 Hourly wind speed; B) Air temperature; C) Wave height in Rivière-Pentecôte and Saint-
883 Ulric (see Fig. 1A for location); D) Water temperature at 22 mab; E) Pressure depth of the
884 ADCP (grey line showing tides and blue dots for 12-h averages) and distance from ADCP
885 to seafloor (red dots) revealing significant change in seafloor depth; F) Vertically-averaged
886 backscatter intensity; G) Along-canyon current velocity at 1.5 mab. Time is in UTC.

887 **Figure 6**. Turbidity current recorded during 15 March 2017: A) Backscatter intensity
888 illustrating the front of the turbidity current; B) Horizontal velocity showing three distinct
889 pulses in velocity and the <5 m thickness of the main near-bed flow, black line is velocity
890 at 1.5 mab; C) Current direction of the turbidity current illustrating the turbulence in the
891 upper flow and homogeneity of flow direction near the seabed; D) Stick plot of current
892 direction and velocity plotted against time and on the seabed (plotted on bathymetric
893 image); E) Interpreted sketch of turbidity current structure. Arrows in the lower layer
894 indicate the alignment of the flow direction compared to the upper layer; F) Wind speed
895 and direction during the turbidity current (shaded area); G) Air temperature; H) Significant
896 wave height in Rivière-Pentecôte and Saint-Ulric; I) Water temperature at 22 mab; J)
897 Pressure depth at ADCP; K) Vertically-averaged backscatter intensity; L) Horizontal
898 velocity at 1 mab. Time is in UTC.

899 **Figure 7**. Turbidity current recorded during 25 January 2017: A) Backscatter intensity
900 illustrating the turbidity current; B) Horizontal velocity showing the <4 m thickness of the
901 main near-bed flow; C) Current direction of the turbidity current illustrating the turbulence
902 in the upper flow and homogeneity of flow direction near the seabed, black line is velocity

903 at 1.4 mab; D) Stick plot of current direction and velocity plotted against time and on the
904 seabed (plotted on bathymetric image); E) Interpreted sketch of turbidity current structure;
905 F) Wind speed and direction during the turbidity current (shaded area); G) Air temperature;
906 H) Significant wave height in Rivière-Pentecôte and Saint-Ulric; I) Water temperature at
907 22 mab; J) Pressure depth at ADCP; K) Vertically-averaged backscatter intensity; L)
908 Horizontal velocity along-canyon at 1 mab. Time is in UTC.

909 **Figure 8**. Comparison of storms generating turbidity currents with those that do not: A-D)
910 Storms with winds that peaked above > 60 km h^{-1} were plotted according to their duration,
911 revealing a significant difference between duration of wind speeds > 60 km h^{-1} for
912 triggering turbidity currents (TC). E-H) Storms that produced > 2 m waves in Rivière-
913 Pentecôte and Saint-Ulric plotted according to their duration.

914 **Figure 9**. Plots of wind speed against tide (A), significant wave height in Saint-Ulric (B)
915 and Rivière-Pentecôte (C) against tide with overlying vector plot for the four storms that
916 triggered turbidity currents. Vector plots start when wind speed reached > 60 km h^{-1} until
917 the turbidity currents were recorded by the ADCP (colored dots). In all four cases, the
918 turbidity currents were triggered when wind speed had diminished and during low (but not
919 exceptionally low) tide.

920 **Figure 10**. Backscatter intensity prior to the turbidity currents during the four events (A-
921 D). Note the increase in backscatter intensity during 25 January and 15 March 2017,
922 interpreted as an increase in suspended sediment.

923 **Figure 11**. Sketch illustrating sediment deposition and erosion observed by the 2016-2017
924 mooring during the two main turbidity currents that led to the migration of crescent-shaped
925 bedforms. A-B) Initial (2016) and final (2017) bathymetry with position of ADCP before

926 and after 15 March 2017; C) Depth profile from 2016 multibeam data along line shown in
927 A; D) Erosion of the lee side and deposition on the stoss side of crescent-shaped bedforms
928 immediately following the 25 January 2017 event; E) Down-canyon (and up stoss-slope)
929 displacement of the mooring during the 15 March 2017 event, and comparison with depth
930 profile from 2017 multibeam data; F-H) 360° seabed profiles around the mooring (*c.* 16 m
931 diameter) computed from the ADCP backscatter intensities; F) Comparison of 360°
932 profiles from ADCP before 26 January 2017 and 2016 multibeam data; G) Illustration of
933 erosion and deposition during the 26 January 2017 turbidity current events (comparison of
934 the 360° profiles before and after the event); H) Illustration of erosion and deposition
935 during the 15 March 2017 event.

936 **Figure 12**. A) Proposed general model for storm-induced turbidity currents in a sediment-
937 starved environment. Note that in other systems, slope failures at canyon heads during
938 storms may be more prevalent than sediment resuspension on the shelf or within the
939 canyons. However, since the shelf consists mostly of bedrock, slope failures cannot account
940 for the triggering of turbidity currents in Pointe-des-Monts. B) Proposed model by which
941 dilute flows ignite by eroding sediment in the upper reaches of the canyon.

942 **Figure 13**. Multibeam bathymetric images of known active canyons and their relationship
943 to sediment supply. A) La Jolla submarine canyon in California, which is fed in sediment
944 by the large Oceanside littoral cell (data used in this image were acquired, archived, and
945 distributed by the Seafloor Mapping Lab of California State University Monterey Bay). B)
946 Monterey Canyon which is fed both by rivers and longshore drift (data used in this image
947 were acquired, archived, and distributed by the Seafloor Mapping Lab of California State
948 University Monterey Bay). C) Squamish delta which is fed by rivers (Conway et al., 2013).

949 D) Pointe-des-Monts canyons which is sediment starved and located adjacent to bedrock
950 and small isolated pocket beaches.

951 **Supplementary figure 1**. Atmospheric and water column measurements for the entire
952 mooring 1 period (3 June 2015 to 1 August 2016); A) Hourly wind speed; B) Air
953 temperature; C) Water temperature at 31 m above bottom (mab); D) Pressure depth of the
954 ADCP; E) Vertically-averaged backscatter intensity; F) Along-canyon current velocity at
955 1 mab. Time is in UTC.

956 **Supplementary video 1**. Animation of seabed changes between 2007 and 2017 in the main
957 canyon of Pointe-des-Monts.

958 **Supplementary video 2**. Animation of seabed changes between 2007 and 2017 in the
959 gullies eats of the main canyon of Pointe-des-Monts.

960 **Supplementary Table 1**. Storms with the strongest wind speeds in Pointe-des-Monts from
961 2015 to 2017. Green highlights those that generated turbidity currents.

962 **Supplementary Table 2**. Storms with the largest significant wave heights in Saint-Ulric
963 from 20 October 2016 and 31 May 2017. Green highlights those that generated turbidity
964 currents.

965 **Supplementary Table 3**. Storms with the largest significant wave heights in Rivière-
966 Pentecôte from 27 October 2016 to 6 June 2017. Green highlights those that generated
967 turbidity currents.

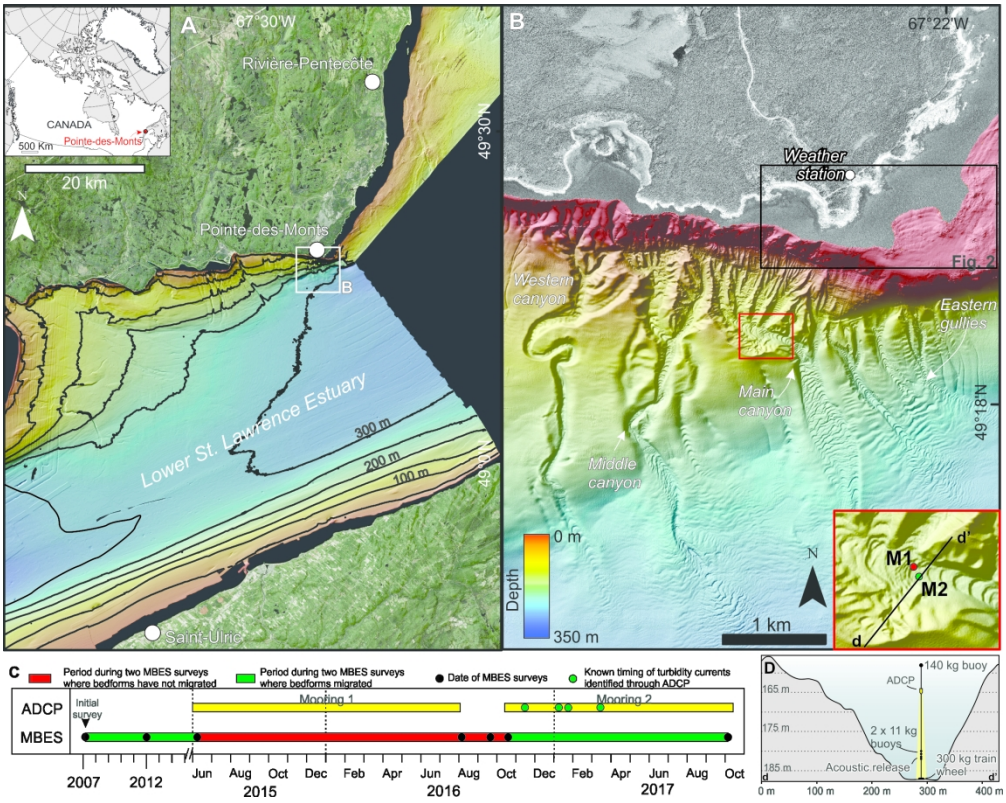

. A) Location of the Pointe-des-Monts turbidite system, Lower St. Lawrence Estuary (eastern Canada). B) Multibeam bathymetry (2012) of the Pointe-des-Monts canyon system with location of moorings 1 (M1, 2015-2016) and 2 (M2, 2016-2017). C) Timeline of the Pointe-des-Monts moorings and bathymetric surveys, including dates of multibeam surveys where bedform migration was observed and ADCP mooring with timing of turbidity currents recorded. D) Design of the second mooring deployed in Pointe-des-Monts that recorded turbidity currents.

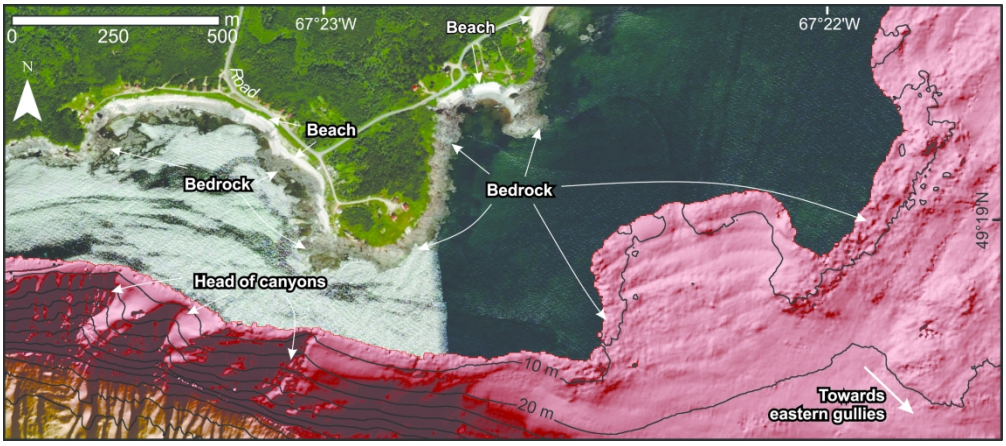

Coastal (satellite imagery) and nearshore geomorphology (bathymetry) illustrating the limited volume of sediment on the shelf and coast. Note the location of bedrock outcrops. Location provided in Figure 1.

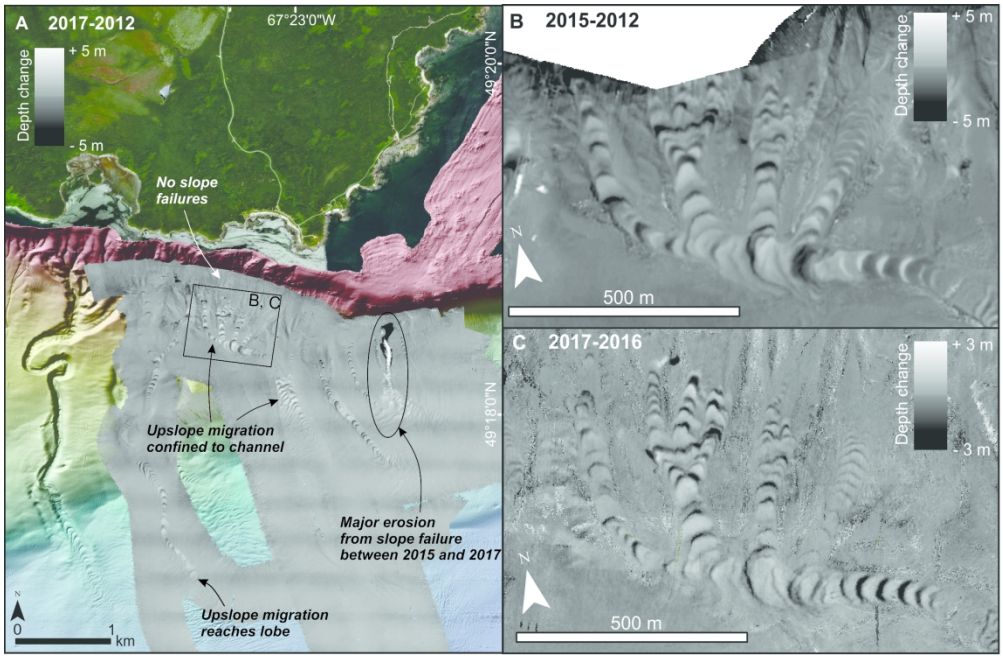

Figure 3. Difference maps of the Pointe-des-Monts canyons: A) 2017-2012 difference map illustrating the upslope migration of cyclic steps in all canyons and gullies; B) 2015-2012 difference map of the main canyon illustrating the lee side erosion and stoss side deposition responsible for the upslope migration of cyclic steps; C) 2017-2016 difference map revealing migration of cyclic steps during mooring 2.

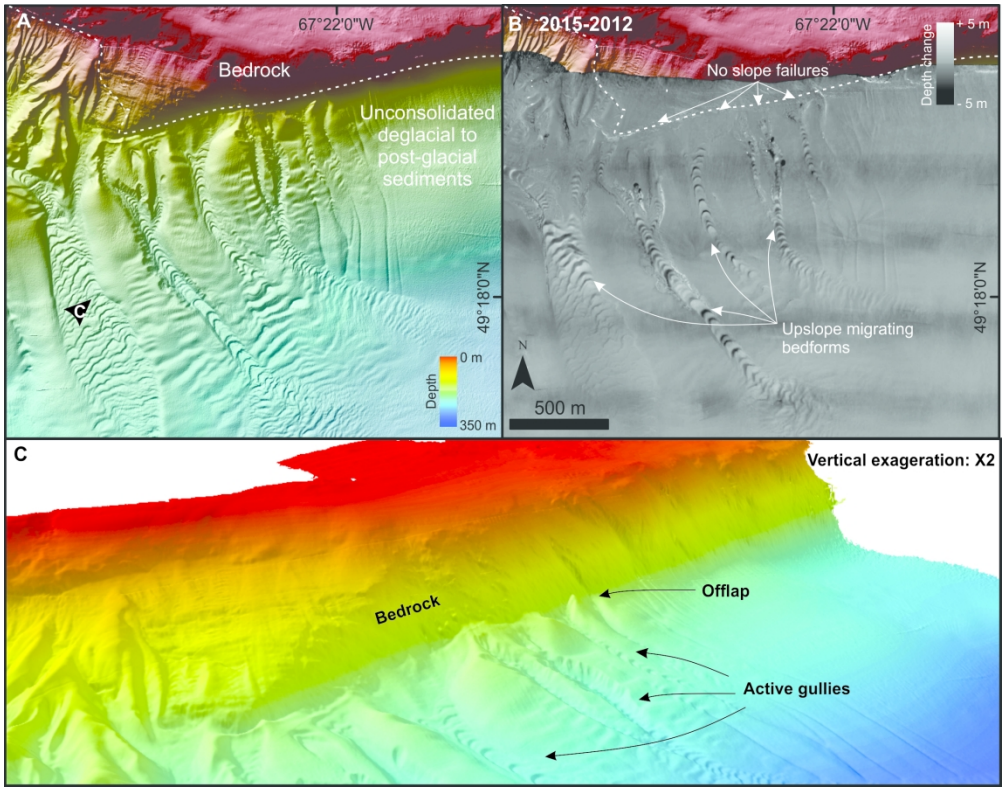

Figure 4. A) Multibeam bathymetry image of the eastern gullies illustrating the unconsolidated post-glacial sediment on bedrock; 2) 2015-2012 difference map illustrating the migration of cyclic steps in the gullies despite no evidence of slope failures during the two years and the absence of sediment on the shelf (see Fig. 2); C) 3D perspective of the eastern gullies offlapping the bedrock slope.

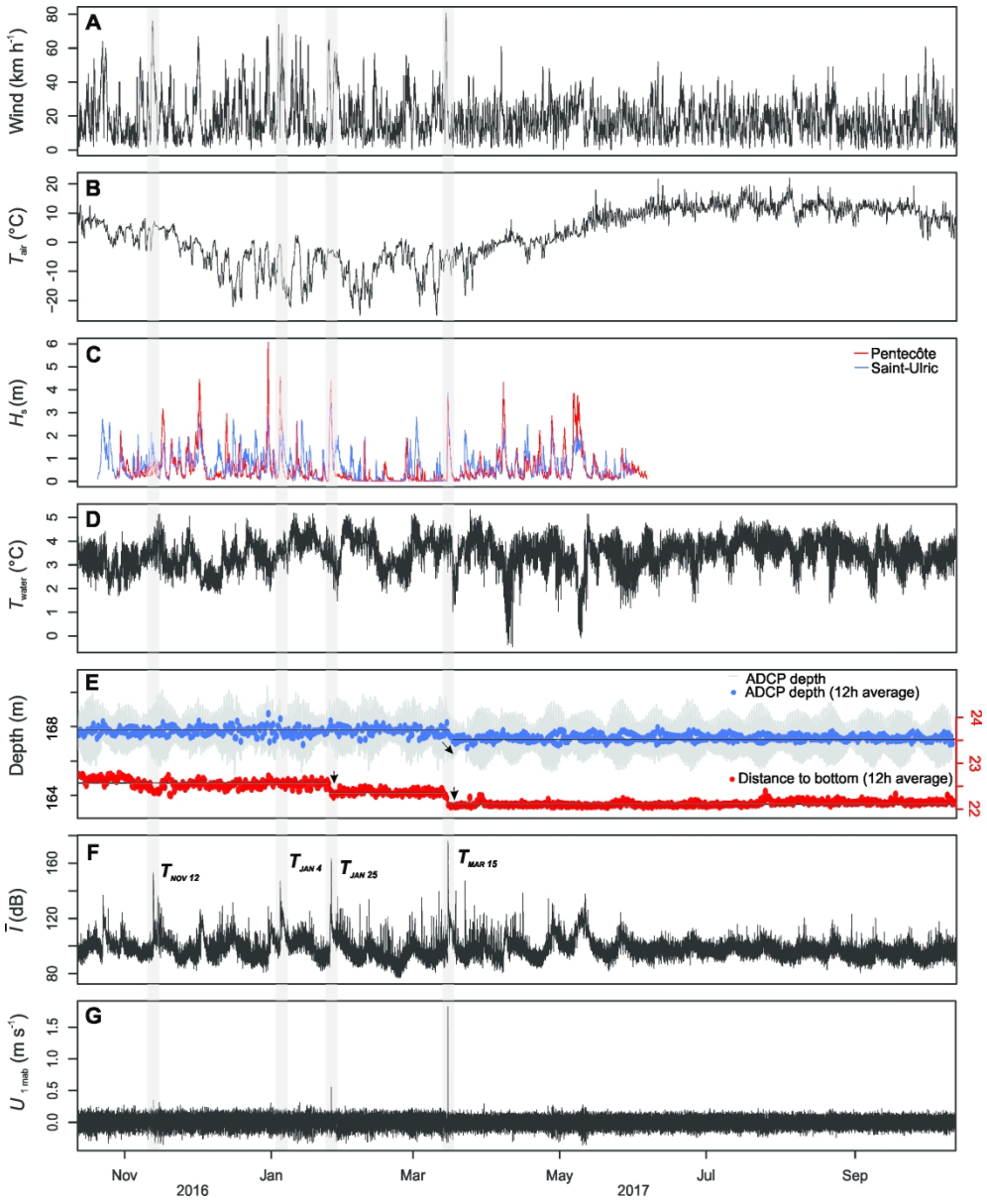

Figure 5. Atmospheric and water column measurements for the entire mooring 2 period (12 October 2016 to 12 October 2017) with four turbidity current events (shaded area): A) Hourly wind speed; B) Air temperature; C) Significant wave height in Rivière-Pentecôte and Saint-Ulric (see Fig. 1A for location); D) Water temperature at 22 mab; E) Pressure depth of the ADCP (grey line showing tides and blue dots for 12-h averages) and distance from ADCP to seafloor (reddots) revealing significant change in seafloor depth; F) Vertically-averaged backscatter intensity; G) Along-canyon current velocity at 1.5 mab. Time is in UTC.

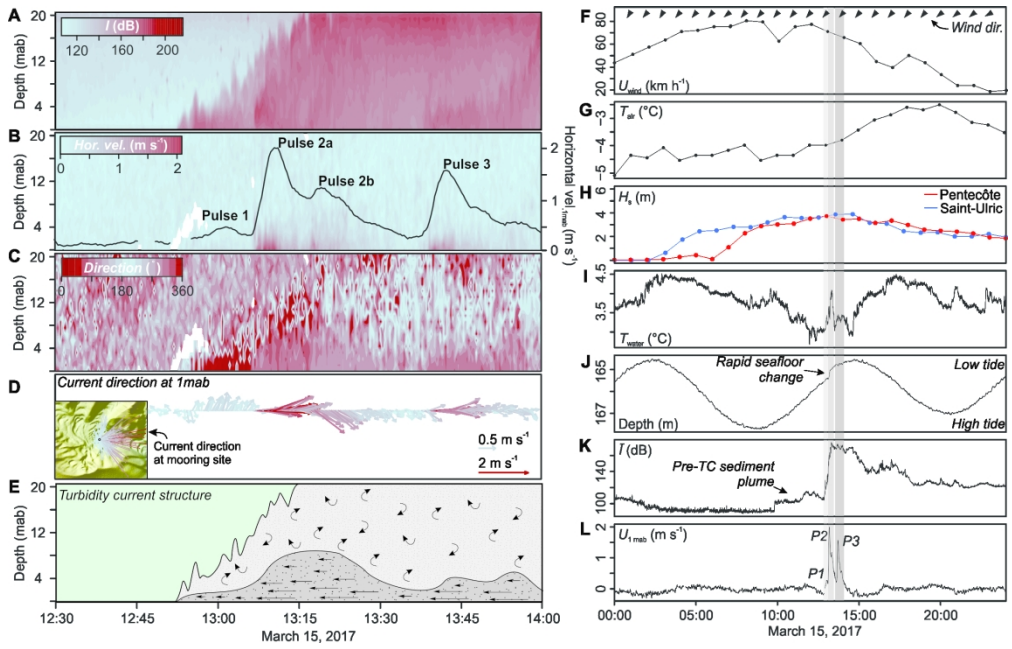

Figure 6. Turbidity current recorded during 15 March 2017: A) Backscatter intensity illustrating the front of the turbidity current; B) Horizontal velocity showing three distinct pulses in velocity and the <5 m thickness of the main near-bed flow, black line is velocity at 1.5 mab; C) Current direction of the turbidity current illustrating the turbulence in the upper flow and homogeneity of flow direction near the seabed; D) Stick plot of current direction and velocity plotted against time and on the seabed (plotted on bathymetric image); E) Interpreted sketch of turbidity current structure; F) Wind speed and direction during the turbidity current (shaded area); G) Air temperature; H) Significant wave height in Rivière-Pentecôte and Saint-Ulric; I) Water temperature at 22 mab; J) Pressure depth at ADCP; K) Vertically-averaged backscatter intensity; L) Horizontal velocity at 1 mab. Time is in UTC.

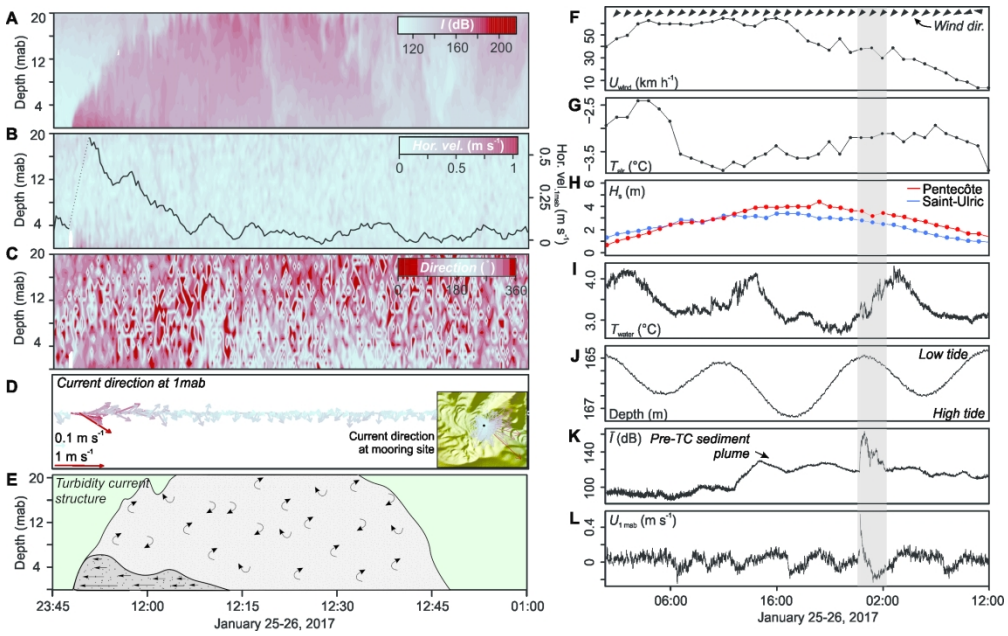

Figure 7. Turbidity current recorded during 25 January 2017: A) Backscatter intensity illustrating the turbidity current; B) Horizontal velocity showing the <4 m thickness of the main near-bed flow; C) Current direction of the turbidity current illustrating the turbulence in the upper flow and homogeneity of flow direction near the seabed, black line is velocity at 1.4 mab; D) Stick plot of current direction and velocity plotted against time and on the seabed (plotted on bathymetric image); E) Interpreted sketch of turbidity current structure; F) Wind speed and direction during the turbidity current (shaded area); G) Air temperature; H) Significant wave height in Rivière-Pentecôte and Saint-Ulric; I) Water temperature at 22 mab; J) Pressure depth at ADCP; K) Vertically-averaged backscatter intensity; L) Horizontal velocity along-canyon at 1 mab. Time is in UTC.

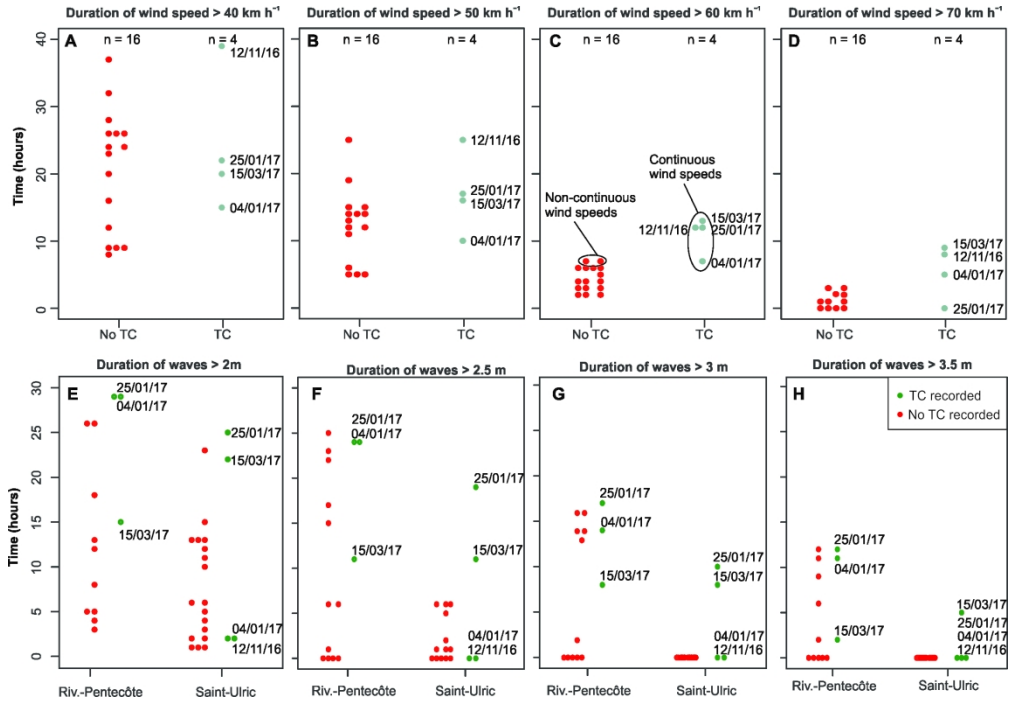

Figure 8. Comparison of storms generating turbidity currents and those that do not: A-D) Storms with winds that peaked above > 60 km h-1 were plotted according to their duration, revealing a significant difference between duration of wind speeds > 60 km h-1 for triggering turbidity currents (TC). E-H) Storms that produced > 2 m waves in Rivière-Pentecôte and Saint-Ulric plotted according to their duration.

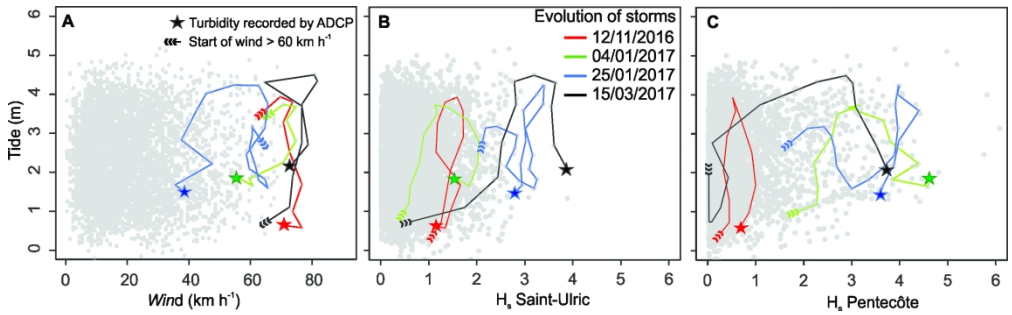

Figure 9. Plots of wind speed against tide (A), significant wave height in Saint-Ulric (B) and Rivière-Pentecôte (C) against tide with overlying vector plot for the four storms that triggered turbidity currents. Vector plots start when wind speed reached > 60 km h-1 until the turbidity currents were recorded by the ADCP (colored dots). In all four cases, the turbidity currents were triggered when wind speed had diminished and during low (but not exceptionally low) tide.

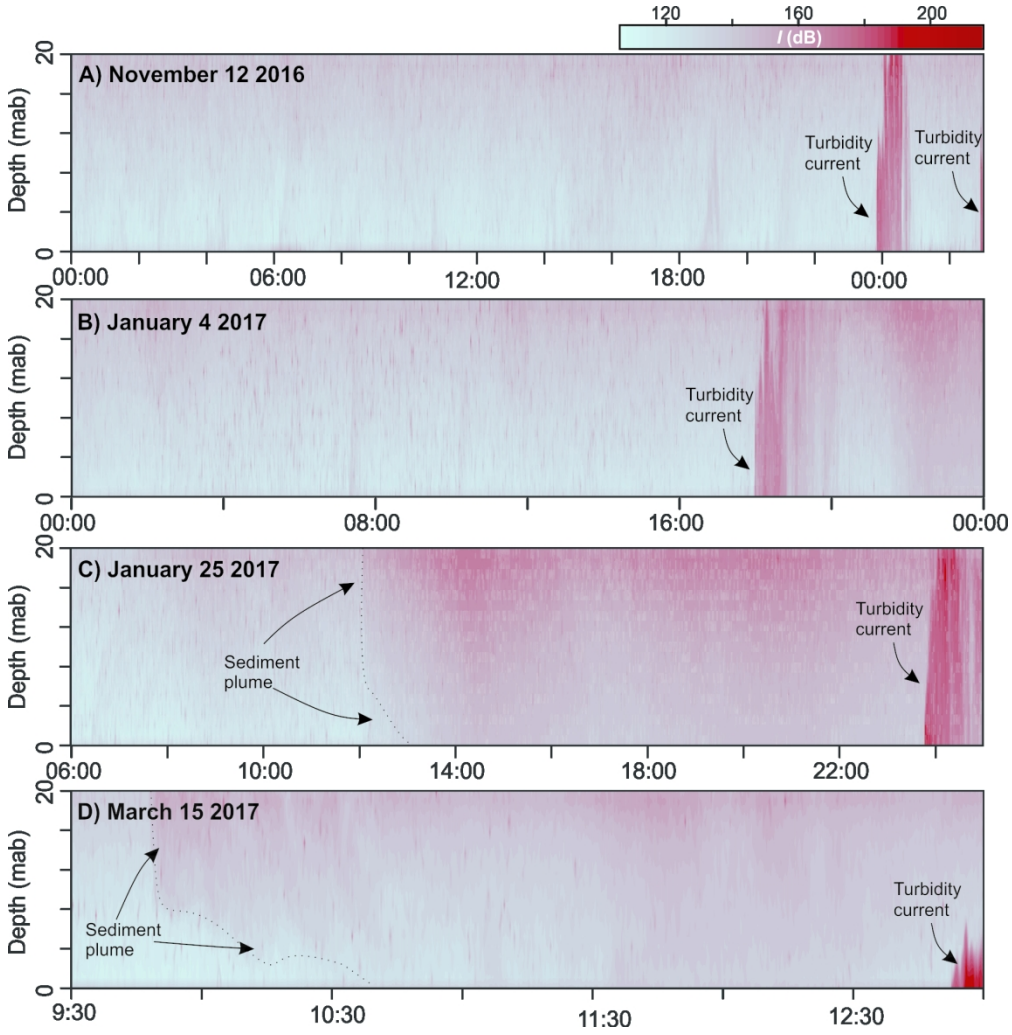

Figure 10. Backscatter intensity prior to the turbidity currents during the four events (A-D). Note the increase in backscatter intensity during 25 January and 15 March 2017, interpreted as an increase in suspended sediment.

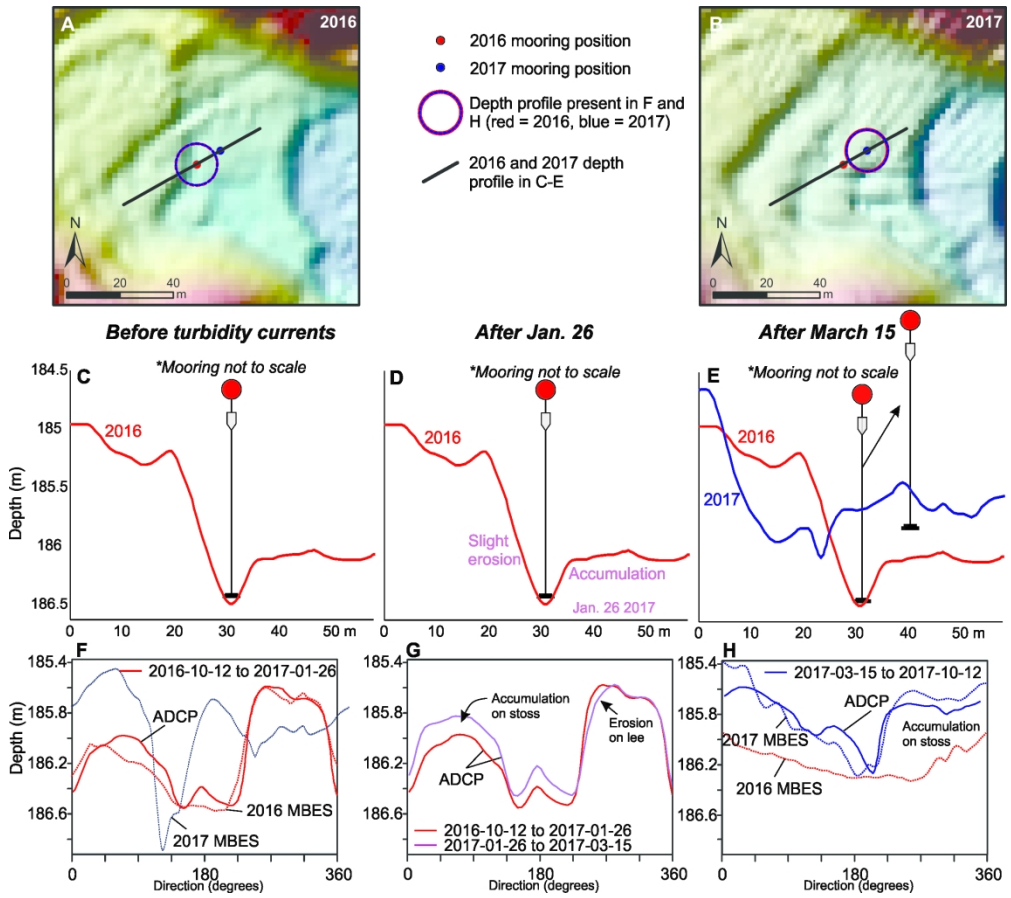

Figure 11. Sketch illustrating sediment deposition and erosion observed by the 2016-2017 mooring during the two main turbidity currents that led to the migration of cyclic steps. A-B) Initial (2016) and final (2017) bathymetry with position of ADCP before and after 15 March 2017; C) Depth profile from 2016 multibeam data along line shown in A; D) Erosion of the lee side and deposition on the stoss side of cyclic step immediately following the 25 January 2017 event; E) Down-canyon (and up stoss-slope) displacement of the mooring during the 15 March 2017 event, and comparison with depth profile from 2017 multibeam data; F-H) 360° seabed profiles around the mooring (c. 16 m diameter) computed from the ADCP backscatter intensities; F) Comparison of 360° profiles from ADCP before 26 January 2017 and 2016 multibeam data; G) Illustration of erosion and deposition during the 26 January 2017 turbidity current events (comparison of the 360° profiles before and after the event); H) Illustration of erosion and deposition during the 15 March 2017 event.

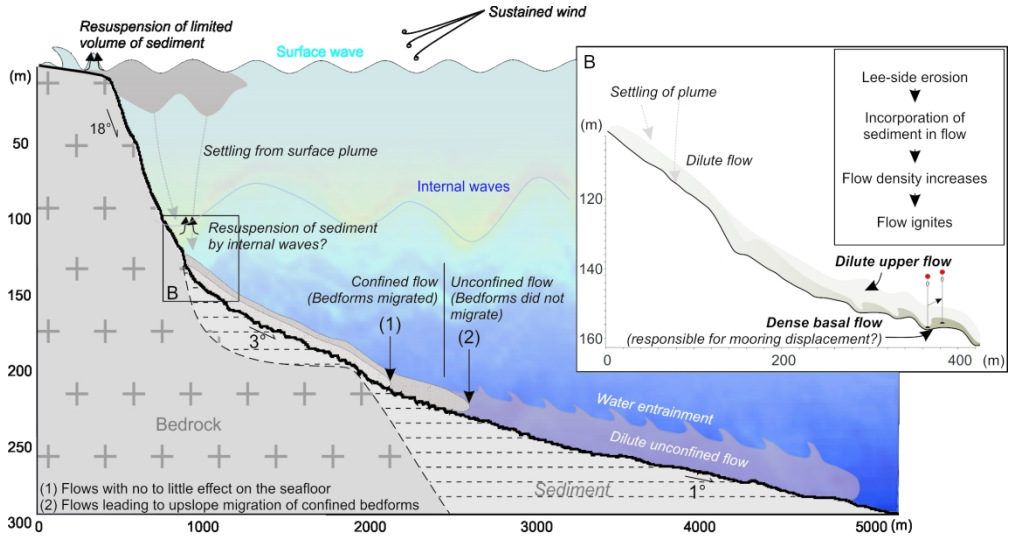

A) Proposed general model for storm-induced turbidity currents in a sediment-starved environment. Note that in other systems, slope failures at canyon heads during storms may be more prevalent than sediment resuspension on the shelf or within the canyons. However, since the shelf consists mostly of bedrock, slope failures cannot account for the triggering of turbidity currents in Pointe-des-Monts. B) Proposed model by which dilute flows ignite by eroding sediment in the upper reaches of the canyon.

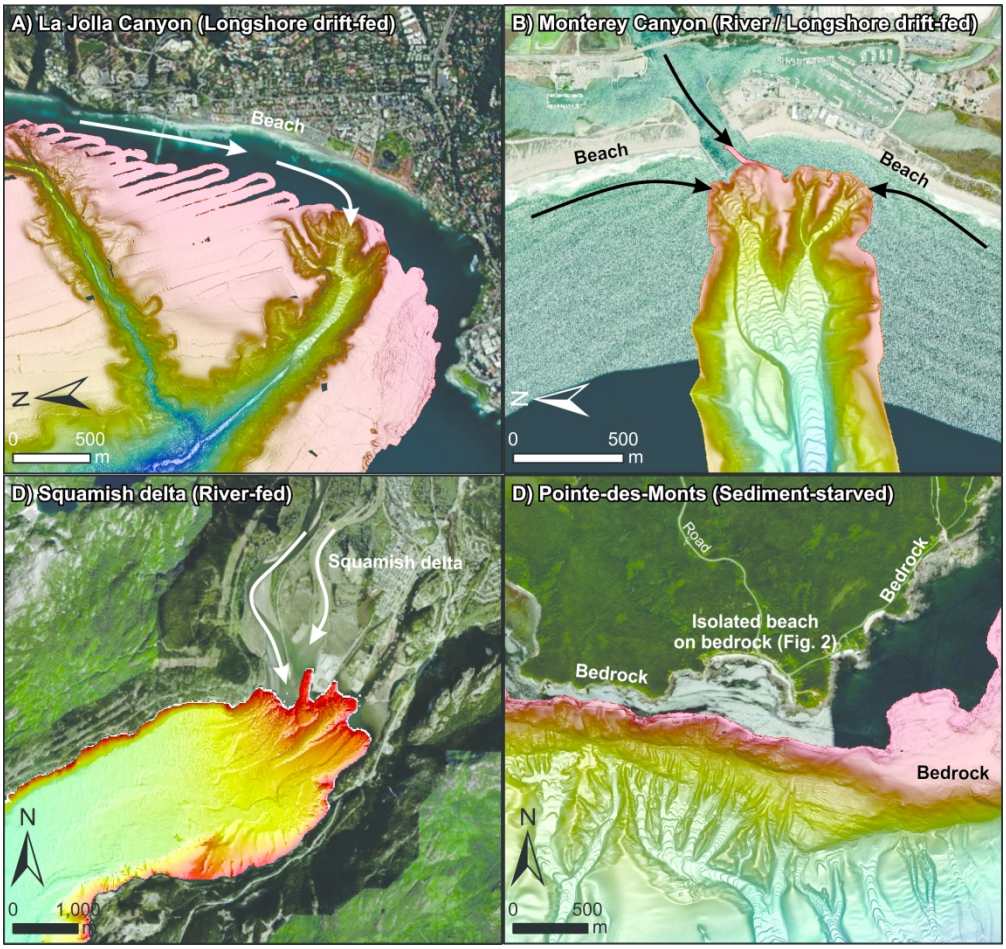

Multibeam bathymetric images of known active canyons and their relationship to sediment supply. A) La Jolla submarine canyon in California, which is fed in sediment by the large Oceanside littoral cell (data used in this image were acquired, archived, and distributed by the Seafloor Mapping Lab of California State University Monterey Bay). B) Monterey Canyon which is fed both by rivers and longshore drift (data used in this image were acquired, archived, and distributed by the Seafloor Mapping Lab of California State University Monterey Bay). C) Squamish delta which is fed by rivers (Conway et al., 2013). D) Pointe-des-Monts canyons which is sediment starved and located adjacent to bedrock and small isolated pocket beaches.

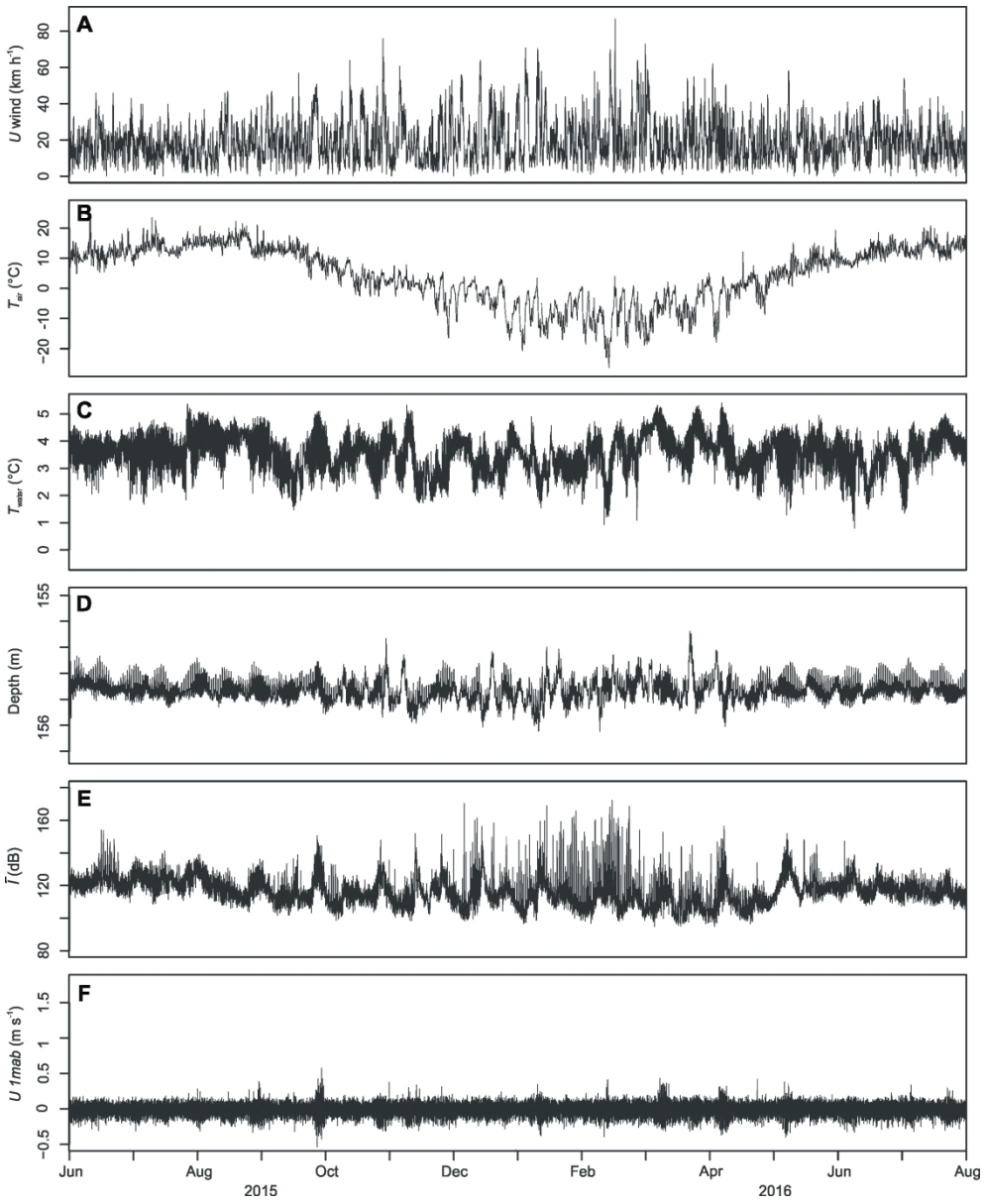
A
U wind (km h-1)
0
20
40
60
80
B
Tair (°C)
−20
-10
0
10
20
C
Twater (°C)
0
1
2
3
4
5
D
Depth (m)
155
156
E
Ī (dB)
80
120
160
F
U 1mab (m s-1)
−0.5
0
0.5
1
1.5
Jun
Aug
Oct
Dec
Feb
Apr
Jun
Aug
2015
2016

Supplementary table 1: Strongest wind speed in Pointe-des-Monts from 2015 to 2017

Rank	Date / Hour (UTC)	Wind speed (km h^{-1})	Direction (°)
1	2016-02-17 09:00	87	240
2	2017-03-15 08:00	81	50
3	2015-10-30 10:00	76	240
4	2016-11-12 21:00	76	240
5	2017-01-04 12:00	74	70
6	2016-03-02 19:00	73	60
7	2016-01-05 23:00	71	240
8	2016-01-11 18:00	71	230
9	2016-02-15 03:00	70	270
10	2017-01-05 23:00	69	260
11	2017-01-11 19:00	68	240
12	2016-12-01 22:00	67	70
13	2016-12-30 14:00	67	50
14	2017-01-13 18:00	67	270
15	2017-10-27 17:00	67	220
16	2017-01-25 11:00	65	40
17	2015-10-14 17:00	64	250
18	2015-12-15 14:00	64	70
19	2016-02-28 05:00	64	230
20	2016-10-23 02:00	64	50

Supplementary table 2: Largest significant wave height in Saint-Ulric from 20 October 2016 and 31 May 2017

Rank	Date / Hour (UTC)	H_{m0} (m)	T_{02} (s)	Dir (°)
1	2017-03-15 14:10	3.88	6.87	29
2	2017-01-25 17:10	3.40	6.49	34
3	2016-12-30 22:10	2.91	5.17	274
4	2017-03-02 11:10	2.82	5.88	30
5	2016-10-22 20:10	2.72	5.71	43
6	2016-12-16 04:10	2.72	5.13	326
7	2017-01-13 15:10	2.7	5.32	280
8	2016-10-25 17:10	2.59	5.77	37
9	2016-12-02 09:10	2.59	5.63	33
10	2017-01-11 20:10	2.58	5.28	272
11	2017-04-17 15:10	2.49	5.37	31
12	2017-04-27 14:10	2.49	5.38	37
13	2017-04-07 19:10	2.34	6.85	31
14	2016-12-25 10:10	2.25	4.63	286
15	2017-03-22 14:10	2.23	4.74	10
16	2017-05-10 02:10	2.22	5.64	34
17	2017-01-05 22:10	2.20	4.65	267
18	2016-11-12 00:10	2.16	4.78	328
19	2016-12-19 05:10	2.05	4.57	278
20	2016-11-06 14:10	2.04	5.31	35

Supplementary table 3: Largest significant wave height in Rivière-Pentecôte from 27 October 2016 to 6 June 2017

Rank	Date / Hour (UTC)	H_{m0} (m)	T_{02} (s)	Dir (°)	Storm surge (m)
1	2016-12-30 16: 10	6.08	7.41	67	1.24
2	2017-01-04 18:10	4.61	6.98	64	0.65
3	2016-12-02 01:10	4.46	6.68	69	0.43
4	2017-01-25 20:10	4.40	7.04	58	0.48
5	2017-04-07 15:10	4.33	6.71	65	0.48
6	2017-05-06 21:10	3.85	7.13	60	
7	2017-05-08 12:10	3.76	6.61	67	
8	2017-03-15 13:10	3.72	6.88	57	0.63
9	2016-11-16 21:10	3.17	6.02	47	0.65
10	2016-12-13 10:10	2.96	6.08	73	
11	2017-04-27 17:10	2.87	5.85	72	
12	2017-01-11 17:10	2.62	5.96	121	
13	2017-05-03 00:10	2.35	5.65	63	
14	2017-04-22 17:10	2.23	5.41	60	
15	2016-10-30 07:10	2.20	5.27	59	
16	2016-11-27 10:10	1.96	4.89	53	
17	2017-02-26 08:10	1.91	5.95	48	
18	2016-11-20 11:10	1.87	4.91	65	
19	2017-02-08 19:10	1.81	7.09	52	0.49
20	2016-12-18 14:10	1.67	5.62	51	